IOPscience iopscience.iop.org

Home Search Collections Journals About Contact us My IOPscience

Self-ordering of Au(111) vicinal surfaces and application to nanostructure organized growth

This article has been downloaded from IOPscience. Please scroll down to see the full text article.

2003 J. Phys.: Condens. Matter 15 S3363

(http://iopscience.iop.org/0953-8984/15/47/009)

View the table of contents for this issue, or go to the journal homepage for more

Download details:
IP Address: 171.66.16.125
The article was downloaded on 19/05/2010 at 17:47

Please note that terms and conditions apply.

INSTITUTE OF PHYSICS PUBLISHING JOURNAL OF PHYSICS: CONDENSED MATTER

J. Phys.: Condens. Matter **15** (2003) S3363–S3392 PII: S0953-8984(03)70844-3

Self-ordering of Au(111) vicinal surfaces and application to nanostructure organized growth

S Rousset[1,2,5], V Repain[1,2], G Baudot[1,2], Y Garreau[3] and J Lecoeur[4]

[1] Groupe de Physique des Solides, Universités Paris 7 et Paris 6, CNRS, 2 Place Jussieu, 75251 Paris Cedex 5, France
[2] Matériaux et Phénomènes Quantiques, FR 2437, CNRS et Universités Paris 7, 2 Place Jussieu, 75251 Paris Cedex 5, France
[3] LURE, CNRS-MRES-CEA, Bâtiment 209D, Centre Universitaire, 91898 Orsay Cedex, France
[4] Laboratoire de Physico-Chimie des Surfaces, CNRS UPRES-A 70-45, ENSCP, 11 rue Pierre et Marie Curie, 75231 Paris Cedex, France

E-mail: rousset@gps.jussieu.fr

Received 22 October 2003
Published 14 November 2003
Online at stacks.iop.org/JPhysCM/15/S3363

Abstract

This paper reports on Au(111) *vicinal* surfaces, either regularly stepped surfaces, reconstructed or not, or periodically faceted surfaces, which are well suited to be used as templates for organized growth of clusters. Angles of misorientation with respect to the (111) plane lie between 1° and 12° and two opposite azimuths are considered: (i) $[2\bar{1}\bar{1}]$, that leads to steps with {100} microfacets, and (ii) $[\bar{2}11]$, that leads to steps with {111} microfacets. The behaviour of the Au(111) reconstruction in the vicinity of steps depends drastically on the step microstructure, and this is a key point for understanding the various periodic morphologies existing on Au(111) vicinal surfaces. The interaction between the reconstruction and the close-packed steps of the Au(111) surface is interpreted in terms of the relative stability of both types of step. Self-organized morphologies between 10 and 100 nm are interpreted within the framework of elastic theory and by pointing out the crucial role played by the atomic boundary energy term. The microscopic origin of faceting is discussed, proposing two different models depending on each azimuth. Then, we illustrate the use of Au(111) vicinal surfaces as templates for growing long range ordered nanostructures. Examples are given in the case of cobalt growth.

1. Introduction

Spontaneous faceting under equilibrium conditions leads to periodic morphologies in the range 1–100 nm. It is an elegant way of nanostructuring semiconductor [1], metal [2] or oxide

[5] Author to whom any correspondence should be addressed.

 © 2003 IOP Publishing Ltd Printed in the UK

surfaces. The faceting phenomenon in which the surface morphology rearranges into a hill-and-valley structure has been known since the turn of the century, as morphology changes were observed on macroscopic metal catalysts by optical methods [3–7]. Then, micron-sized facets were observed by electron microscopy, for example on copper crystal surfaces under oxygen absorption [6]. Theoretical work identified the faceting origin early as due to the surface free energy anisotropy and a link with the equilibrium shape of crystallites was established [8, 9]. From a phase transition point of view, the analogy between the break-up of a surface into a hill-and-valley morphology and the phase separation of a binary solution is now well established. In the case of faceting, the surface orientation, or the step density, plays the same role as does the concentration in describing the binary fluid phase separation, and a number of orientational phase diagrams have been successfully proposed for vicinals of Au(100) [10], Pt(100) [11] and Si(113) [12, 13].

Since the step density is the order parameter to describe the faceting of clean surfaces, the surface free energy can be written as a general development versus the step density. If θ is the vicinal angle, i.e. the angle of misorientation with respect to the close packed surface defined by $\theta = 0$, L the terrace width and h the step height, $\tan\theta = h/L$ is proportional to the step density. Thus the surface free energy projected on the reference plane $\theta = 0$ can be written as

$$\gamma(\theta) = \gamma_0 + \frac{\beta}{h}|\tan\theta| + \delta|\tan\theta|^2 + g|\tan\theta|^3 \tag{1}$$

where some of these terms are clearly understood [14]. γ_0 is the surface free energy of the (111) reference plane, β is the step free energy and g is the step–step interaction. These three terms, together with a repulsive interaction between steps ($g > 0$), describe the surface free energy of a regular stable vicinal surface. However, other terms are necessary in order to explain the faceting instability and various microscopic mechanisms lead to their existence. For example, the presence of a surface reconstruction also leads to faceting. Indeed, in a general way, a reconstruction induces that γ_0, β and g are functions of the vicinal angle θ. The most famous example is the (7×7)–(1×1) transition where the Si(111) vicinal surfaces misoriented towards the $[\bar{2}11]$ direction are faceted for temperatures below the phase transition [15, 16]. The phase separation between a reconstructed (7×7) Si(111) facet and a non-reconstructed stepped phase has been interpreted as a loss of convexity of the surface free energy when the surface free energy curves for the reconstructed and unreconstructed structures intersect. In the case of Au(100) [17, 18, 10] and Pt(100) [11] the observation of faceting has been interpreted in terms of local minima in the surface free energy, called magic vicinals, when the terrace width is commensurate or nearly commensurate with the reconstruction, leading to the possibility of optimal registry [19].

In the case of Au(111) vicinal surfaces, there are two experimental facts that strongly indicate that they should be unstable towards faceting: (i) the gold equilibrium crystal shape displays sharp edges around the facets and (ii) the Au(111) surface is reconstructed.

The macroscopic observation of gold equilibrium crystal shape (ECS) has been obtained after deposition on two different substrates, either graphite [20, 21] or α-SiC [22] and examined by scanning electron microscopy. All these experimental investigations agree on the fact that gold ECS displays discontinuous facet to vicinal transitions. This appears as sharp edges around both the (111) and (100) facets. More recently, the interpretation of such a shape has been revisited by Bonzel *et al* [23] by adding the fourth term in equation (1). Although the link between the macroscopic ECS and the microscopic interpretation of the surface free energy development of a vicinal surface is not yet understood, sharp edges clearly mean that Au(111) vicinal surfaces are unstable towards faceting. This result is also confirmed by observation of sharp edges on periodic profiles annealed at 1023 K [24] or by determining the faceting morphologies of Au(111) stepped surfaces either by using x-ray scattering [25–27] or scanning

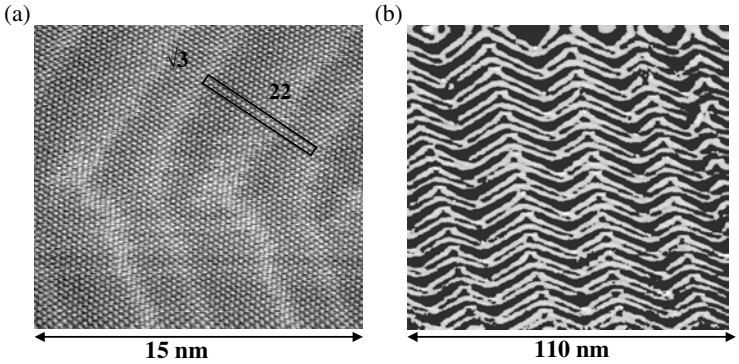

Figure 1. Two STM images zooming out the reconstruction of Au(111). (a) Atomic resolution showing the $22 \times \sqrt{3}$ reconstruction of the Au(111) surface. Corrugation is 0.3 nm. The rectangular unit cell is drawn. (b) The secondary herringbone reconstruction seen on a larger area, also called the chevron phase. White lines are discommensuration lines.

tunnelling microscopy (STM) [28, 29, 2]. It is worth noting that Au(111) vicinals have also been studied under an electrochemical environment [30, 31].

The microscopic origin of the Au(111) vicinal faceting instability has to be searched for in the famous $22 \times \sqrt{3}$ reconstruction of the Au(111) surface [32–34]. This reconstruction has been described within a Frenkel–Kontorova (FK) model [35–38]. It involves a non-uniform compression of the surface atoms along the $[1\bar{1}0]$ direction, with domain walls, also called linear discommensurations, separating surface regions with the correct (fcc) stacking from regions with a faulted (hcp) stacking sequence (see figure 1(a)). Each discommensuration incorporates an additional one-half of an atom relative to the bulk (111) planes. The periodicity between faulted regions ($L_{\mathrm{D}} = 65$ Å) corresponds to 22 atoms. The reconstructed layer is 4% denser than the bulk (111) planes. Further energy minimization of a very small strain energy associated with the anisotropy of the stress relief in the $22 \times \sqrt{3}$ reconstruction leads to a secondary reconstruction pattern called the herringbone reconstruction or the chevron phase [34, 39, 40], of which the periodicity is about 300 Å (see figure 1(b)). The thermal behaviour of Au(111) was investigated using x-ray scattering [41–43]. The periodicity of the $22 \times \sqrt{3}$ reconstruction seems to exist at any temperature studied (from 300 to 1250 K, the melting temperature of gold being 1337 K) [41, 42]. However above 865 K, the herringbone reconstruction loses long range order, and a first-order phase transition is completed at 880 K. The high temperature phase is called a discommensuration fluid phase. As far as we know no link has been established between this phase transition and the faceting morphology of Au(111) vicinal surfaces.

One difficulty comes from the fact that introducing steps on the surface changes the microscopic structure of the reconstruction. For example, as soon as the vicinal angle is larger than one degree, the herringbone reconstruction cannot exist any longer since the periodicity of this reconstruction is larger than the terrace width. Therefore, any investigation of the role played by the reconstruction on the stability of Au(111) vicinals should start with a systematic study of the influence of steps on the reconstruction. We will report on such a study in section 3.

The paper is organized as follows. The next section details the experimental preparation of Au vicinals under ultra-high vacuum conditions and the techniques (mainly a combination of scanning tunnelling microscopy (STM) and grazing incidence x-ray diffraction (GIXD)) used for determining both the macroscopic and the atomic structures of the surfaces. All the sample

Table 1. {100} step vicinal surfaces: summary of the nominal angles of misorientation θ, number of atomic rows in each terrace n and terrace widths W. The Miller indices are $(n+1, n-1, n-1)$ and the terrace width is calculated using $W = (n - 1/3) * 0.25$.

	θ (deg)	n	W (nm)
Au(12, 11, 11)	2.38	23	5.7
Au(11, 9, 9)	5.57	10	2.4
Au(433)	8.05	7	1.7
Au(755)	9.45	6	1.4
Au(322)	11.4	5	1.2

orientations studied are also summarized in this experimental section. Section 3 elucidates the interaction between close-packed steps and reconstruction as studied directly by STM on a Au(111) sample. Section 4 is devoted to the experimental determination of Au(111) *vicinal* morphology, i.e. both the atomic structure and the long range order. In section 5, interpretation of the experimental results is given concerning the faceting origin of Au(111) vicinals. Two different models for explaining the microscopic origin of Au(111) vicinal faceting are explained depending on which azimuth surfaces are cut. Finally, a phase diagram is proposed in section 6 for these surfaces and we summarize the existence of known magic vicinals. Section 7 focuses on the interpretation of the long range order found on the faceted surfaces. The interplay between atomic order and mesoscopic order is studied within the framework of Marchenko's model [44]. The role played by the edge energy is highlighted in this section. Finally, section 8 shows how Au(111) vicinals can be used for growing organized nanostructures.

2. Experimental details

2.1. Au samples

Except for the study presented in section 3, which has been performed by using a Au(111) single crystal, all samples are Au(111) vicinal surfaces which are single crystals cut by spark erosion to produce discs of either 4, 9 or 12 mm in diameter and 2 mm in thickness, depending on each sample. Many different samples have been studied, but all of them are cut within the $[0\bar{1}1]$ zone axis. Thus all steps are parallel to this close-packed $[0\bar{1}1]$ direction since gold is a face-centred cubic (fcc) crystal. Two opposite azimuths have been investigated (see figure 2). For vicinals oriented towards $[\bar{2}11]$, steps exhibit {111} microfacets; this is the case for Au(11, 12, 12), Au(788), Au(455), Au(577) and Au(233). We have also investigated morphologies of Au(12, 11, 11), Au(11, 9, 9), Au(433), Au(755) and Au(322) which are oriented towards $[2\bar{1}\bar{1}]$, whose steps exhibit {100} microfacets. The crystallographic parameters of these surfaces such as the angle of misorientation θ, the number n of atomic rows in each terrace and the corresponding terrace widths are summarized in tables 1 and 2. Angles of misorientation with respect to the reference plane Au(111) range between 2° and 12°.

2.2. Experimental procedure

The sample *ex situ* preparation is described elsewhere [30, 2]. Once introduced into the UHV chamber, with a base pressure of 3×10^{-11} mbar, the sample is prepared using repeated cycles of sputtering with argon ions (typically at an argon pressure of 5×10^{-5} mbar, and a voltage of 600 V) and annealing at 800 K. Observations are made *in situ* by STM experiments. STM images were taken first with a home-made microscope [28, 29], then with a variable temperature STM from Omicron.

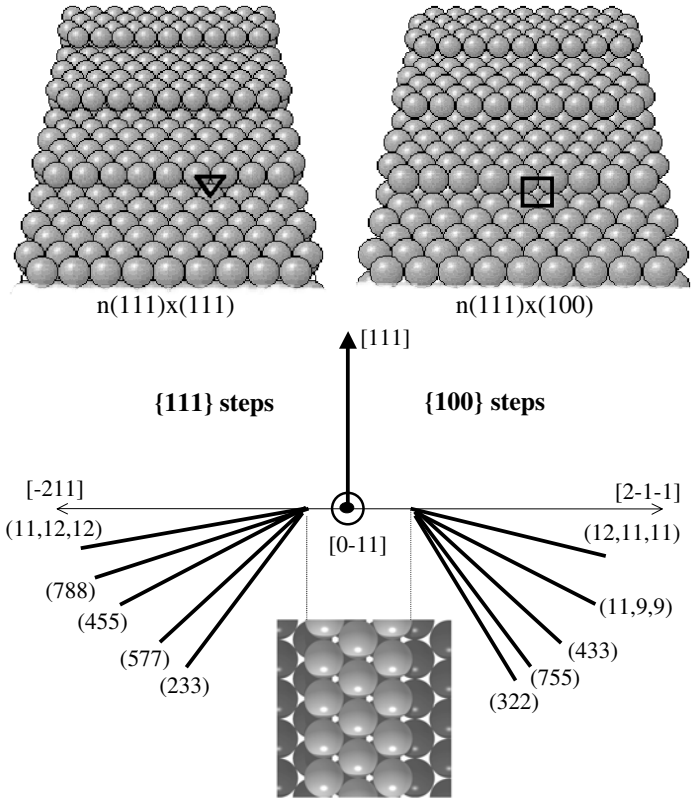

Figure 2. Schematic diagram of Au(233) and Au(322) surfaces which are characteristic of Au(111) vicinal surfaces studied in this paper: $n(111)\times(111)$ i.e. with a miscut angle along the $[\bar{2}11]$ azimuth ($\{111\}$ type steps) and $n(111)\times(100)$ i.e. with a miscut angle along the $[2\bar{1}\bar{1}]$ azimuth ($\{100\}$ type steps). n is the number of atomic rows in each terrace. The bottom of the drawing summarizes the nominal vicinal planes studied in the paper regarding the azimuth.

Table 2. $\{111\}$ step vicinal surfaces: summary of the nominal angles of misorientation θ, number of atomic rows in each terrace n and terrace widths W. The Miller indices are $(n-2, n, n)$ and the terrace width is calculated using $W = (n-2/3) * 0.25$.

	θ (deg)	n	W (nm)
Au(11, 12, 12)	2.27	24	5.83
Au(788)	3.51	16	3.83
Au(455)	5.76	10	2.33
Au(577)	8.47	7	1.58
Au(233)	10.0	6	1.33

GIXD experiments were performed in a UHV diffractometer on beam line DW 12 at LURE-DCI (Orsay). The macroscopic surface normal is aligned with the diffractometer rotation axis ω in order to keep the incident angle constant at a critical angle ($\sim$0.3° for wavelength 0.827 Å) during the scans and using Z-axis geometry. The vicinal orientation was checked *in situ* by localization of Bragg peaks and the corresponding vicinal angle was taken into account in the program for using the hexagonal coordinate system for the (111) fcc terrace structure, described in the next paragraph.

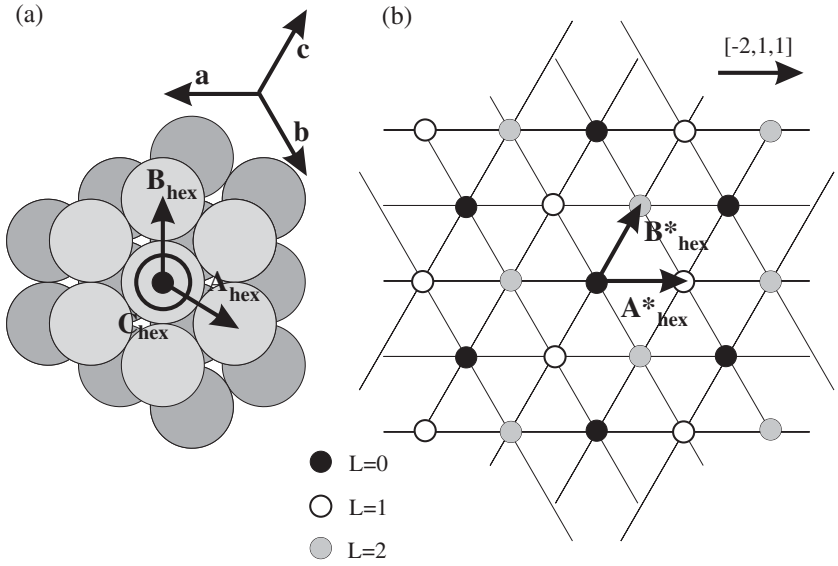

Figure 3. (a) Surface (111) where the lattice vectors are drawn. (b) Schematic diagram of the reciprocal space.

All crystallographic directions (*hkl*), mentioned here, are defined in the conventional cubic coordinate system describing the fcc gold crystal with lattice parameter $a = 4.08$ Å. However, the (111) atomic planes of an fcc crystal are hexagonally close packed. It is therefore convenient to employ a hexagonal coordinate system when describing the scattering from a (111) fcc surface. The reciprocal axes (**A***, **B***, **C***) are deduced from a hexagonal coordinate system in real space with vectors (**A**, **B**, **C**) drawn in figure 3. Vectors **A** and **B** are in the terrace plane with $A = B = a/\sqrt{2} = 2.88$ Å, whereas **C** is along the perpendicular $[111]_{\text{cubic}}$ direction, with $C = 3h = 7.05$ Å, h being the step height, $h = a/\sqrt{3} = 2.35$ Å. In the reciprocal space (see figure 3(b)), $A^* = B^* = 4\pi/\sqrt{3}A = 2.52$ Å^{-1} for the (H,K) plane normal to the $[111]_{\text{cubic}}$ direction and $C^* = 2\pi/C = 0.89$ Å^{-1} for the L index. In this coordinate system, the hexagonal reciprocal space indices H, K and L are related to the conventional cubic indices h, k and l by the transformations $H = -h/2+k/2$, $K = -k/2+l/2$ and $L = h+k+l$. The component of the scattering vector in the $(111)_{\text{cubic}}$ plane is determined by H and K, while the out-of-plane scattering vector is given by L. Since the hexagonal unit cell in real space (**A**, **B**, **C**) is not primitive, bulk Bragg peaks do not appear for each integer value of L, but they should satisfy the condition $2H + K + L = 3n$, which leads to a periodicity of $3C^*$ along the **C*** axis, as can be seen in figure 3(b).

Once the gold surface is well prepared, cobalt evaporation is performed using a 2 mm diameter cobalt rod directly heated by electron bombardment ($I_{\text{em}} = 12$ mA, $HV = 800$ V). The pressure during the process is below 2×10^{-10} mbar. Typical flux rate is 1 ML min^{-1}. The flux calibration is made using an *in situ* quartz microbalance.

3. Interaction between steps and reconstruction on Au(111)

Stepped surfaces often exhibit properties which depend on the interactions between steps and reconstructions [14]. In this section we report on a systematic behaviour between the close-packed steps on Au(111) and the $22 \times \sqrt{3}$ reconstruction. This result, of particular interest

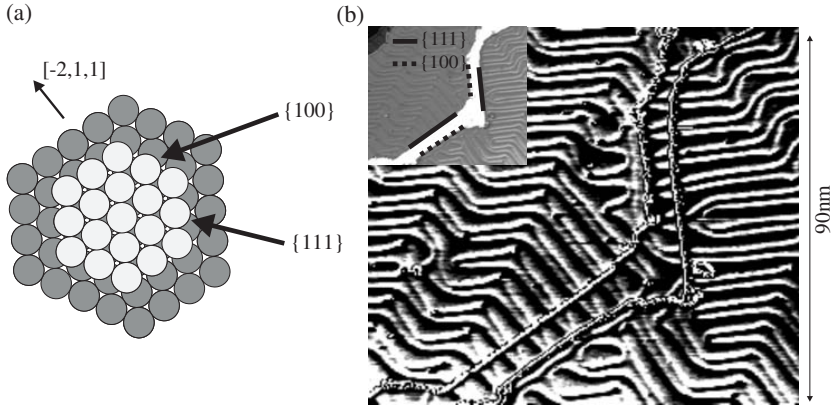

Figure 4. (a) Schematic top view of a (111) surface showing two atomic levels and both kinds of close packed steps. One is made of a {111} microfacet and the other of a {100} microfacet. (b) STM image of a Au(111) surface. Size is 100 nm × 90 nm. The image is recorded at $T = 150$ K. The corrugation due to the terrace levels has been subtracted in order to enhance the reconstruction lines. Inset is the raw image which displays the atomic grey levels. Four terraces are clearly seen, each one associated with a grey level and one being a plateau crossing the whole image from bottom left to the upper right. {111} steps are indicated by full lines and {100} ones by dotted lines. Orientation of steps is consistent with (a) (from [46]).

for managing new nanostructured substrates, is interpreted in terms of the relative stability of both types of step.

The $22\times\sqrt{3}$ reconstruction is easily recognized on STM images by the presence of stacking fault lines which are lines of highest corrugation on the surface, also called discommensuration lines. It has been observed on Au(111) [34] that these lines are very often found perpendicular to the steps. However, discommensuration lines which do not correspond to a usual compression direction also exist, parallel to the step edges [34]. STM experiments performed on a Au(111) surface demonstrate that this behaviour can be unambiguously associated with the atomic structure of steps [45, 46]. Two types of close-packed step can be found on a (111) surface. A descending step along the $[\bar{2}11]$ azimuth presents a {111} microfacet, whereas an ascending step along the same azimuth is made of a {100} microfacet (see figure 4(b)). We have indeed found on some wide Au(111) terraces a monatomic height plateau which gives the opportunity to observe on the same image both types of close-packed step. Indeed, two opposite steps along the same azimuth have a different atomic structure (see figure 4). As seen in figure 4, when the discommensuration lines cross an ascending step, they are no longer present on the other side of the plateau. Moreover, a discommensuration line parallel to the step edge is found at the bottom of the corresponding descending step. This effect can be systematically attributed to the type of step, since it is clear that when the steps are rotated by 60° the effect is reversed. Indeed, a rotation of 60° exchanges the crystallographic structure of the steps (see figure 4). A Laue x-ray diffraction pattern allows us to attribute unambiguously one type of step to each structural effect.

When the step is crossed by the lines of the reconstruction (which is the effect usually known), it is made of a {111} microfacet. On the other hand, when the step is, *a priori*, made of a {100} microfacet, the bottom of the step encounters a line of stacking fault parallel to the step edge. Knowing that the smallest area on the $22\times\sqrt{3}$ reconstruction corresponds to hcp stacking, atoms closest to the descending step edge are in fcc sites. This is easily understood since these atoms are closest to the atoms underneath the step which are in the bulk stacking. Moreover, atomic resolution of a step edge clearly shows that the stacking fault associated

with the reconstruction remains unchanged until the last atomic row of the upper terrace [45]. Thus, the initially {100} microfacet structure of a step is transformed into local portions of {111} microfacet where the upper atoms are in hcp sites. In contrast, the atomic structure of an initially {111} step edge remains unchanged when it is crossed by the discommensuration lines. These results strongly suggest an energetic interpretation for the observed behaviour. For metals like gold or platinum, the step energy of {111} type steps has been found to be lower than that of {100} type steps [47]. This can be easily understood if one considers the atomic density of each kind of step. Thus, the behaviour of the reconstruction in the vicinity of steps, which is described above, can be interpreted as a way of minimizing the step energy of an initially {100} step edge.

Once first observed, we checked that this effect was systematically found on numerous areas of the surface where steps are present [46]. In addition, we have intentionally fabricated both types of step on the Au(111) surface by making holes with ion argon sputtering. It has been demonstrated [48] that a layer-by-layer removal regime can be found when the Au(111) surface is sputtered at a temperature between 120 and 220 °C. In this regime, two-dimensional islands of surface vacancies are formed, hexagonal in shape and one layer deep. Therefore, they display both types of step, as can be seen in figure 5. As shown in figure 5, the reconstruction is present everywhere around the holes, although strongly disordered due to the high density of steps in all directions. More interesting is the way the reconstruction can be found at the bottom of these vacancy islands. The most systematic structural effect is that one edge of the hexagon out of every two is crossed by discommensuration lines, perpendicular to it. By comparing the orientation of the hexagon with the preceding observations, edges crossed by the reconstruction lines can be unambiguously attributed to {111} type steps. As previously discussed, it is clear that atoms closest to the bottom of {100} type steps are in fcc stacking. Again, the existence of the reconstruction on the top of the step edge transforms locally the step in portions of the {111} microfacet and thus lowers its energy. As visible in figure 5, due to the complex arrangement of reconstruction between the holes, it sometimes happens that the discommensuration lines do not reach the top of a {111} step. Then there is no reconstruction at the bottom of the corresponding step edge. This behaviour is consistent with our energetic argument which favours keeping the {111} step structure unchanged. Additional proof of such an interaction between reconstruction and steps can be found in experiments that we have performed on single crystals with Au(111) vicinal surfaces and that will be described below in the next section.

4. Equilibrium morphology of Au(111) vicinals

In this section we report on structural determinations of Au(111) vicinal equilibrium morphologies. The reasons for interpreting these morphologies as equilibrium ones are the following.

(i) Hundreds of preparation cycles on all surfaces have been performed, until the morphology no longer evolves. Indeed, faceted surfaces exhibited different morphologies at the very beginning.

(ii) The annealing time was also varied from a flash up to 48 h without any modification observed at room temperature.

(iii) The cooling rate has been varied from a natural flash to a slow rate (a few hours for cooling down to room temperature). The evolution of the morphology from the highest temperature of annealing has been followed with x-rays and shows that the cooling rate has no effect and that the faceting morphology evolves with temperature in a reversible way for temperature above 700 K [26].

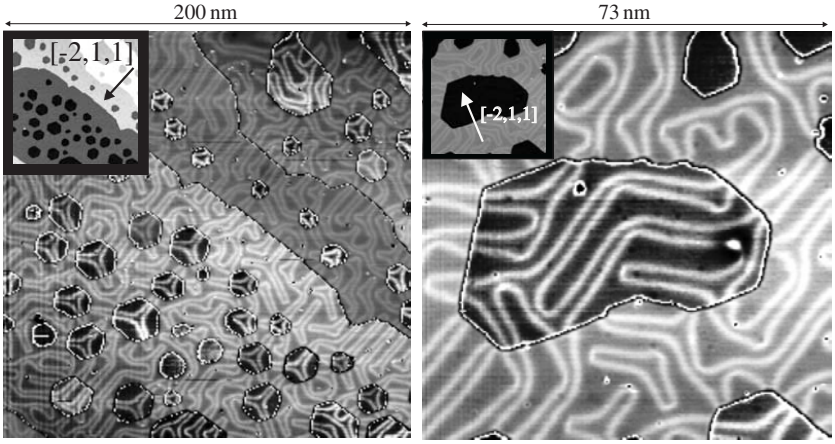

Figure 5. STM images of a Au(111) surface; argon ions sputtered at 200 °C. (a) Inset, raw STM image showing four atomic levels and the vacancy islands bounded by monatomic steps. The same image is shown where the corrugation due to the terrace levels has been subtracted in order to enhance the reconstruction lines. (b) STM image of a few vacancy islands. $T = 300$ K. Inset, the raw STM image. The same image is shown where the corrugation due to the terrace levels has been subtracted in order to enhance the reconstruction lines (from [46]).

4.1. Structure of stable vicinals

Stable vicinals of Au(111) can be divided into two classes depending on whether the terraces are reconstructed or not.

4.1.1. Stable unreconstructed vicinal surfaces: Au(322), Au(755) and Au(233). Au(322), Au(755) and Au(233) surfaces have been investigated using both STM, low-energy electron diffraction (LEED) and GIXD. Their morphology is similar to an atomic staircase, where steps are all one atom high ($h = 0.235$ nm), and equally spaced across the surface. STM images allow precise determination of terrace width histograms. The Au(322) substrate is misoriented by an angle of 11.4° along the $[2\bar{1}\bar{1}]$ azimuth and displays monatomic steps regularly spaced with an averaged terrace width distribution of 1.2 nm (see figure 6). No reconstruction is seen on such a surface. LEED and GIXD measurements also suggest that there is no reconstruction. The Au(755) surface is cut in the same azimuth as the (322) surface. It is also a regular stepped surface without any reconstruction. The Au(233) surface has the same number $n = 6$ of atomic rows in each terrace as the Au(755) surface but it is misoriented in the opposite azimuth. Angles of misorientation with respect to the (111) plane are concentrated around 10° for all three stable unreconstructed surfaces. When the surfaces investigated display a much smaller misorientation angle, i.e. about 4° or below, terraces become reconstructed.

4.1.2. Stable reconstructed vicinal surfaces: Au(788) and Au(11, 12, 12). Au(788) and Au(11, 12, 12) are stable regularly stepped surfaces, with monatomic steps like the former vicinals. But now all terraces are reconstructed, as can be determined both using STM images and GIXD spectra. The Au(788) surface is misoriented by 3.5° with respect to the (111) orientation towards the $[\bar{2}11]$ azimuthal direction. The step crystallographic structure is $\{111\}$ and each terrace contains 16 atomic rows (see figure 7(a)). After the surface preparation, the sample displays 10 μm defect free areas with a roughness < 1 nm. It shows all over the

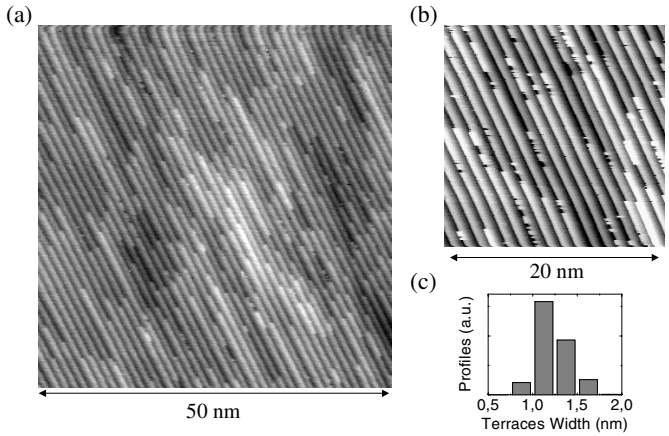

Figure 6. (a), (b) STM images of the Au(322) surface. All steps are monatomic in height. (c) Terrace width distribution. The statistics has been done over 15 images and 30 000 widths.

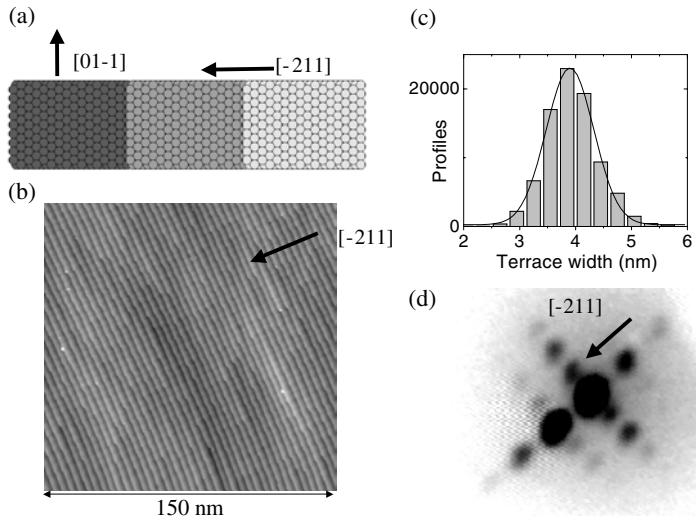

Figure 7. (a) Schematic top view of a (788) non-reconstructed surface. Steps are 0.235 nm high and close packed. The crystallographic structure of the step edge is a $\{111\}$ microfacet. Terraces are (111) planes and consist of 16 atomic rows. The terrace width is 3.83 nm and the associated miscut angle with respect to the (111) plane is 3.52° towards the $[\bar{2}11]$ azimuthal direction. (b) STM image of our single-crystal (788) sample. It displays a very regular and straight step array. (c) Terrace width distribution of the (788) surface measured over 40 different images and 80 000 terrace profiles. The Gaussian fit (full curve) is centred at 3.9 nm and has a full width at half maximum of 0.85 nm. (d) LEED pattern of the specular spot taken at $E = 23$ eV (from [90]).

surface a regular pattern of monatomic steps, 0.235 nm high (see figures 7(b) and (c)), with a terrace width distribution centred at 3.9 nm and with a 0.85 nm full width at half maximum. The surface is reconstructed and discommensuration lines run perpendicular to the step edges, in agreement with the systematic behaviour of the reconstruction found in the vicinity of $\{111\}$ microfaceted steps, as shown in section 3. However, it should be pointed out that the periodicity of the reconstruction along the steps is greater on the vicinal area than on wide

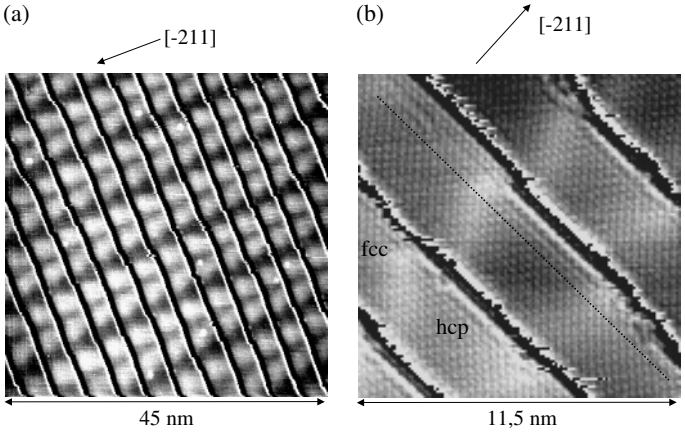

Figure 8. STM images of the Au(788) surface. The corrugation due to the terrace levels has been subtracted in order to enhance the reconstruction lines. (a) At large scale, the discommensuration lines are running perpendicular to the step edges. However, within a terrace, they display a 'V' shape. (b) Atomic resolution image. The dotted line is a guide to the eye to observe the fcc to hcp stacking transition through a discommensuration line. No surface dislocation can be found on this surface structure (from [90]).

Au(111) terraces, in agreement with the fact that steps partially relieve stress. The LEED pattern (see figure 7(d)) indicates the good long range order (on a macroscopic scale) of both the stepped surface and the reconstruction since we can see up to the third diffraction peak order in both directions. Due to the presence of steps, the discommensuration lines are disturbed and no longer run perpendicular to the close-packed direction. Indeed, it can be seen from the images that, instead of being perfectly parallel over the whole terrace, these lines form a 'V' shape within terraces (see figure 8(b)). As a consequence, following the observation made on a Au(111) surface near a $\{111\}$ step [46], the fcc domain width decreases approaching the upper part of the step (see figure 8). This is consistent with the fact that the fcc domain should be larger near the bottom of the step since it is the bulk stacking of gold. It is worth noting that the exact atomic arrangement near the step edge is not known. How the hcp surface stacking changes into an fcc stacking in the bulk is still an open question.

The Au(11, 12, 12) surface, which is misoriented with respect to Au(111) by a vicinal angle of 2.31°, displays a similar behaviour to the Au(788) surface. Terrace width distribution has been measured from STM images over 30 images and 200 terraces. It is quite narrow since about 60% of the terrace widths equal the average terrace width value $\langle L \rangle = 5.8$ nm [49].

From a nanostructuration point of view, these surfaces are patterned in two dimensions at a nanometre scale:

(i) along the $[\bar{2}11]$ direction, the periodicity is the terrace width and is linked to the miscut angle [50];

(ii) along the $[01\bar{1}]$ direction, the periodicity is 7.2 nm, fixed by the reconstruction, and does not vary significantly with the miscut angle.

Such patterned substrates at a nanometre scale have been successfully used in order to serve as a template for two-dimensional long range ordered growth of uniform cobalt nanostructures [51]. This will be shown in the last section of this paper.

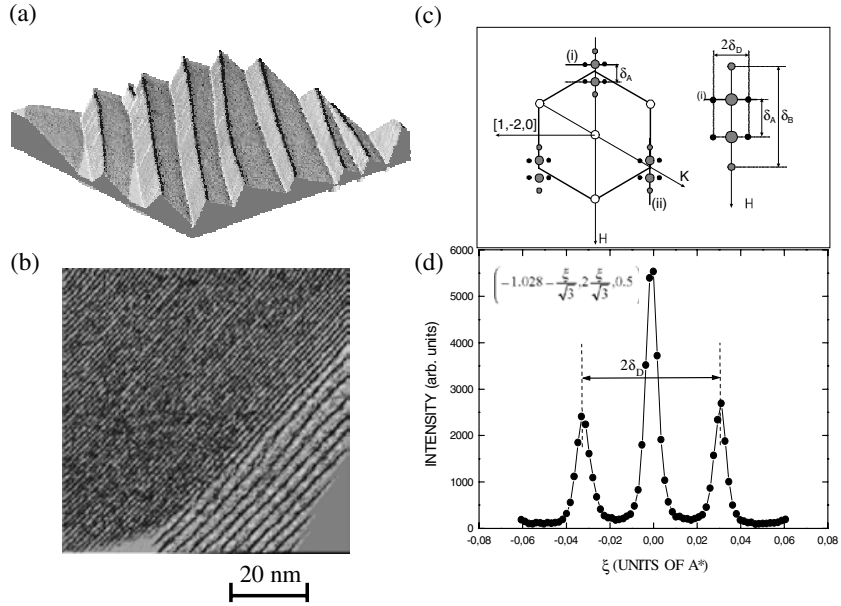

Figure 9. Faceted morphology of Au(455). (a) Three-dimensional STM image of the faceted Au(455) showing the long range order of the hill-and-valley morphology. The scan area is 1.4 μm $\times$ 1.4 μm. (b) STM image zooming in on a frontier between facets. All steps are monatomic, of height 2.35 Å. (c), (d) X-ray scattering results obtained on the faceted Au(455) surface. (d) Transverse scan obtained on the faceted Au(455) surface along the [1, -2, 0] direction, showing two satellites, separated by a distance $2\delta_D$. A schematic diagram of the projected reciprocal space in the (H, K) plane is displayed in the upper part. (i) is the position of the scan shown below. (ii) is the direction of a typical H-scan showing the quadruplet drawn in grey. Satellites of phase A are indicated by small black dots.

4.2. Morphology and atomic structure of faceted vicinals

4.2.1. Results on unstable vicinals with {111} step edges. Two vicinal surfaces, Au(455) and Au(577), have been investigated. When the surface undergoes a specific preparation under electrochemical environment [30, 26], prior to *in situ* UHV treatment, a periodic array of monatomic steps (2.3 Å high) is readily found on Au(455) and Au(577), in close resemblance with the ideal bulk termination. After the UHV *in situ* treatment described in the experimental section above, the hill-and-valley structure is obtained on both surfaces (see figure 9(a)). Zooming on the hill-and-valley morphology reveals that both sides are portions of stepped surfaces (see figure 9(b)) whose terrace widths are $w_A = 31 \pm 3$ Å and $w_B = 12 \pm 1$ Å. The corresponding vicinal angles with respect to (111) are $\theta_A = 4°$ and $\theta_B = 10°$. The 10° facet is the Au(233) which is one of the stable surfaces described above. The determination of this orientation is even more precise than what we can measure from STM images. Indeed, the fact that Au(577) is faceted, although its misorientation angle is very close to that of Au(233) (see table 2), is the best proof that Au(233) must be exactly the orientation corresponding to the smallest terraces found on both Au(455) and Au(577) [52]. For Au(455) STM images reveal that the faceted morphology presents a super-periodicity of about 180 nm (see figure 9(a)). The extent of each phase is found, using statistical analysis of STM images, to be 80 nm for the 10.0° phase and 100 nm for the 4.0° phase. For Au(577) the period was found to be 260 nm and the extents L_A and L_B of phases A and B are $L_A = 80$ nm and $L_B = 180$ nm.

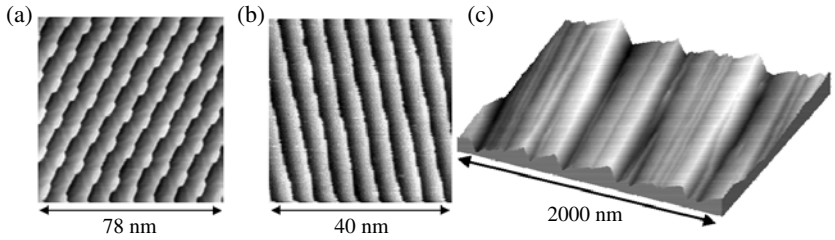

Figure 10. STM images of the Au(12, 11, 11) surface. (a) STM image of one vicinal facet (large terraces) of the Au(12, 11, 11). (b) STM image of the other vicinal facet (small terraces) of Au(12, 11, 11). (c) 3D view of Au(12, 11, 11) faceted morphology.

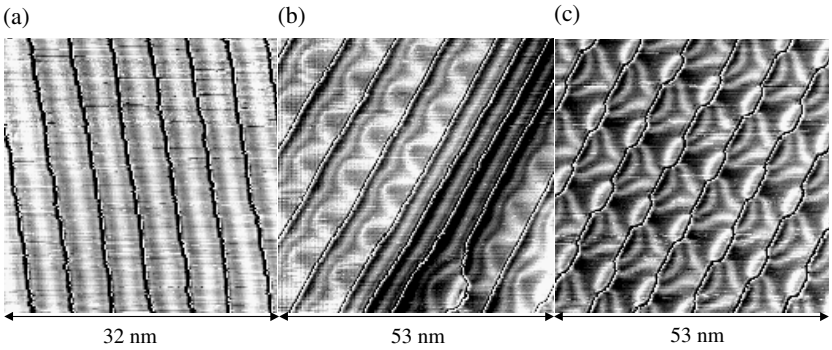

Figure 11. STM images of the Au(12, 11, 11) surface where the corrugation due to the terrace levels has been subtracted in order to enhanced the surface reconstruction. (a) Small terrace vicinal facet: one discommensuration line is running parallel to the steps. (b) Large terraces next to small ones. The reconstruction on the large terraces exhibits a 'viaduct' pattern. (c) Large terraces away from the border with small terraces. The reconstruction pattern induces a periodic super-kink array.

It is worth noting that the 4.0° orientational phase is close to the previous (788) surface. Moreover, all terraces of this phase are found to be reconstructed with lines of discommensurations crossing the steps perpendicularly. This has been demonstrated using STM images, LEED patterns [29] and GIXD [26]. Each vicinal facet gives rise to a specific splitting of LEED spots at a given energy, as expected for a uniformly stepped surface. As a consequence, diffraction spots for the faceted morphology are indeed quadruplets as in figures 9(c) and (d). The spacing of inner spots (respectively outer spots) reflects the vicinal period of phase 1 (respectively phase 2). In addition, figures 9(c) and (d) show that satellites of phase 1 spots are visible along the $[0\bar{1}1]$ direction. The related period in real space is about 7 nm. This reconstruction is consistent both with what is observed on Au(111) surface STM images [34, 45], where the $\{111\}$ steps are crossed perpendicularly by the discommensuration lines, and the findings of the stable reconstructed Au(788) and Au(11, 12, 12) surfaces.

4.2.2. Results on vicinals with $\{100\}$ step edges. Let us first examine the morphology of a vicinal surface misoriented towards $[2\bar{1}\bar{1}]$ by a 2.38° angle. The Au(12, 11, 11) surface phase separates into two different stepped areas forming a hill-and-valley morphology. The long range order distance of the hill-and-valley structure is about 500 nm, as shown in figure 10(c). Zooming into the facets exhibits that both facets are reconstructed vicinal portions with different terrace widths (see figures 10(a) and (b)). The smallest terraces which display a $\langle L \rangle = 4.56$ nm average exhibit a white line of higher corrugation in the middle of each terrace, and parallel to the step edge (see figure 11(a)). This reconstruction is in remarkable agreement with findings

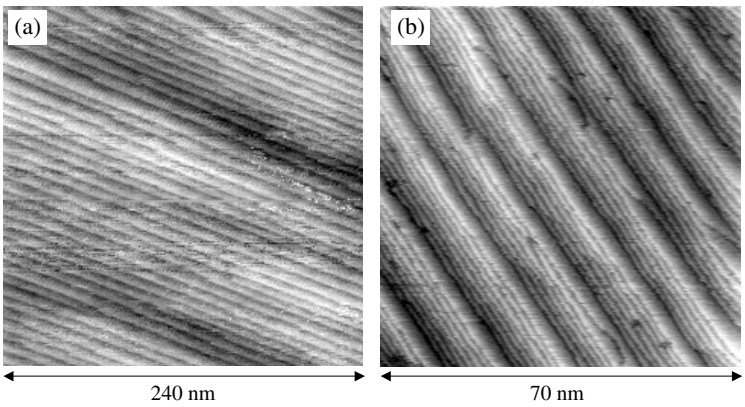

Figure 12. STM images of the Au(433) faceted surface. (a) Large scale STM image of Au(433). Only the super-periodicity is resolved at this scale. (b) STM image of a smaller Au(433) area where all atomic steps are clearly seen.

on the interaction between steps and reconstruction deduced from STM images taken on a Au(111) surface (see section 3).

The largest terraces found on the Au(12, 11, 11) faceted morphology have an $\langle L \rangle = 8.23$ nm average width, corresponding to a 1.6° misorientation with respect to (111). Their atomic structure is quite complicated. Two different structures have been observed in the same conditions. The first one (see figure 11(b)) consists in one line parallel to the steps and followed by periodic arches. We will refer to it as the 'viaduct' structure. Such a structure is found in the vicinity of a facet edge. The second structure (see figure 11(c)) was not reported before, but it is a nice example of what patterns are formed in order to minimize the sum of the surface and step energies. Indeed, the 'viaduct' structure does not transform many portions of {100} into {111} microfacets. In order to change a larger proportion of steps, the discommensuration line should cross a {100} step edge. However, we have never observed such a crossing. Instead, the steps are faceted by presenting periodic super-kinks made of {111} microfacets large enough to be crossed by a stacking fault line. The complete structure of this reconstruction is difficult to describe accurately but it leads to an almost complete transformation of the {100} step edge into a less energetic {111} step edge.

Increasing the misorientation angles, we have investigated two vicinals Au(11, 9, 9) and Au(433) whose angles are between 4° and 9°. The first surprising result is that, although two different terrace widths are found all over the surface, a very small faceting periodicity is found. For Au(433), one large terrace (width $w_A = 4.0$ nm) separates on average six steps so that the overall morphology displays a periodicity of $D = 11.5$ nm (see figure 12). The short terraces display a 1.4 nm average width. For Au(11, 9, 9) a stable morphology is found consisting of a periodic succession (period about 7 nm) of one large terrace (width $w_A = 4.2$ nm) followed by one or two short terraces ($w_B = 1.4$ nm) (see figure 13). Short terraces both in Au(433) and Au(11, 9, 9) have the same value consistent with that of Au(755) which has been found to be stable. The interpretation of the presence of larger terraces which are of similar width for these two surfaces but also very close to the value of the smallest terraces of the faceted Au(12, 11, 11) was not straightforward since no reconstruction was seen on STM images of both Au(433) and Au(11, 9, 9). GIXD was the most powerful technique in determining the exact atomic structure in this case, as explained below.

The presence or not of a reconstruction on Au(11, 9, 9) was resolved by GIXD measurements [2]. We used the hexagonal ($H\,K\,L$) coordinate system convenient for the (111)

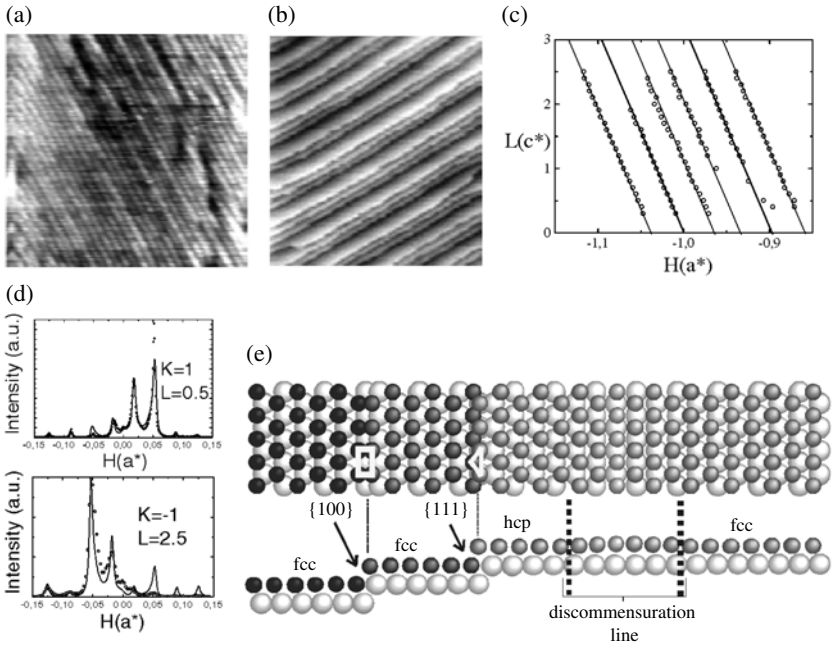

Figure 13. Morphology and atomic structure of Au(11, 9, 9). (a) Large scale STM image of Au(11, 9, 9). The area is 200 nm × 200 nm, where about 40 super-periods are clearly visible. Atomic steps are not resolved. (b) STM image of a smaller Au(11, 9, 9) area (40 nm × 40 nm) taken under UHV where all atomic steps are clearly seen. (c) L positions versus H of the main peaks observed in the H-scans at $K = 2$. Straight lines are guides to the eyes. (d) The open circles display typical GIXD H-scans recorded at anti-Bragg conditions but for different values of K and L. Lines display the calculated spectra deduced from our model. (e) Schematic top view (upper part) and side view (lower part) of the atomic structure showing the surface reconstruction on the large terrace. The {100} step (respectively {111} step) has been highlighted by a white rectangle (respectively triangle). The stacking sequence of topmost atoms, hcp or fcc, is indicated above each terrace.

fcc terrace structure [26], recalled in section 2. Performing H-scans (scans perpendicular to the step edge) at different L-values (the L-direction is perpendicular to the terraces) reveals that all diffraction rods are parallel and oriented perpendicular to the macroscopic surface (see figure 13(c)). The slope of the rods (5.7°) and the distance between them giving a periodicity of 6.9 nm are both consistent with the expected morphology shown in figure 13(b). However, experimental spectra, all obtained by scanning in the anti-phase conditions but at different positions of the reciprocal space, drastically differ in their intensity distribution (see figure 13(d)). On the Au(11, 9, 9) surface, we did not observe any satellite peak characteristic of the usual Au(111)-22 × $\sqrt{3}$ reconstruction. Following our findings on the interaction between steps and reconstruction on a Au(111) surface, we developed an atomic model of the surface in order to reproduce the GIXD spectra. This model includes a discommensuration line parallel to the step edges on the larger terraces, which respects the surface symmetry but which is not in any usual direction known for the 22 × $\sqrt{3}$ reconstruction. This line is similar to what is observed on the small terraces of the faceted Au(12, 11, 11) surface (see figures 11(a) and (b)). In our model, atoms of the large terraces which are near the descending step are in hcp sites whereas those near the ascending step are in fcc sites (see figure 13(e)). The smaller terraces remain unreconstructed. Our model also includes two different arrangements found within the super-period, i.e. whether the large terrace is followed

by one (structure 1) or two (structure 2) short terraces (see figure 13(b)). The terrace widths w_1 and w_2, as well as the proportion p of structure 2, have been determined by statistics over STM images. The proportion p of structure 2 is found to be about 70%. Thus, the model contains three parameters: the correlation coefficient q of the ordering between the two structures ($q = 0$ corresponds to completely segregated phases and $q = 1$ corresponds to a random mixture between the two structures), the width and the position of the discommensuration line. As shown in figure 13(d), the introduction of the discommensuration line accounts for the strongly different spectra obtained in the anti-phase condition, and the agreement between the experimental data (open circle) and the calculated spectra (full curve) is excellent. Parameters deduced from the calculations are the following: $q = 0.45$, the discommensuration line width is six atoms and the fcc (respectively hcp) stacking domain on the large terrace contains seven (respectively five) atomic rows (see figure 13(e)). Although this reconstruction is unusual, it is again consistent with previous works on the Au(111) surface [45]: a discommensuration line is systematically observed parallel to the step edge at the bottom of {100} steps whereas {111} steps are always crossed by discommensuration lines. This was interpreted by a step energy minimization. This effect is even more important in the case of the Au(11, 9, 9) surface. Indeed, the descending step edges of the larger terraces are transformed into {111} step edges (see figure 13(e)) which is known to be energetically favourable. The particular behaviour of the reconstruction is thus strongly governed by step energetic arguments. It should also be mentioned that the existence of such stacking fault lines has been suggested on a Pt(111) vicinal surface with {100} steps [53].

4.3. Summary of Au(111) vicinal morphology

Both the mesoscopic order (periodically faceted or not) and the atomic structure (reconstructed terraces or not) are elucidated on all surfaces.

The determination of atomic structure on each terrace is one of the most crucial issues. Results described above suggest that there is a critical angle θ_c such that for $\theta > \theta_c$ stable vicinals are not reconstructed, whereas for $\theta < \theta_c$ stable vicinals display reconstructed terraces. This result is consistent with the fact that steps partially relieve stress. θ_c is comprised between 4° and 9°. The reconstruction is similar to the well known reconstruction of Au(111) in the sense that fcc stacking areas are separated from hcp areas by discommensuration lines. However, different morphologies of the reconstruction are found depending on the azimuth and the terrace widths. When the steps are made of {111} microfacets, the stacking fault lines always cross the steps perpendicularly. The line periodicity slightly varies with respect to the terrace width: 7.9 nm for 3.3 nm wide terraces and 7.2 nm for 3.8 nm whereas a 6.3 nm period is known for the infinite (111) terrace. When the steps are made of {100} microfacets, the discommensuration line structure depends on the terrace width. For 4 nm wide terraces a line of discommensuration is found to be parallel to the step edge. When terraces are larger, more complex structures are reported. We have shown that the driving force for these morphologies is the minimization of the step energy, the {111} microfaceted step being more stable than the {100} microfaceted one.

One of the most original results is the self-organized morphology found on Au(111) faceted surfaces. Au(11, 9, 9) and Au(433) display small periods of respectively 7 and 11 nm, whereas Au(12, 11, 11), Au(577) and Au(455) present 500, 260 and 180 nm periods respectively. Thus faceted surfaces are indeed able to provide self-organized patterned substrates in the range between 1 and 100 nm, which might be of interest for further use of these substrates as templates for epitaxial growth. Regarding the faceting phenomena, it is questionable to interpret Au(11, 9, 9) and Au(433) morphology as a faceted one, since the phases are very

small to be real thermodynamic phases. We try to elucidate this point in the next section by developing models for faceting in Au(111) vicinals.

5. Microscopic origin of faceting in Au(111) vicinal surfaces

In this section, we will explain that the reason for faceting of {100} microfaceted stepped surfaces is mainly the terrace energy modulation explained by an FK model, whereas we suggest that faceting of {111} microfaceted stepped surfaces is due to a competition between the step energy term and the terrace energy term. In these models the reconstruction is always the driving force for the faceting transition but the exact atomic structure is linked to the different models.

5.1. Frenkel–Kontorova model of faceting for vicinals with {100} step edges

In the case of {100} step vicinal surfaces, we have found the existence of either one terrace or a complete vicinal area showing a reconstruction with one discommensuration line parallel to each step. This occurs when the terrace width is about 4 nm (4.2 nm on Au(11, 9, 9) and 4.6 nm on Au(12, 11, 11)). Now we justify the stability of such a phase by thermodynamics arguments.

Since the microscopic structure of the discommensuration line (see figure 13(e)) found on Au(11, 9, 9) consists of a purely uniaxial compression in the direction perpendicular to the step edges, it allows us to develop a one-dimensional model to explain the faceting properties. The stressed terrace energy per unit area E_1 is calculated as a function of the terrace width L using an FK model [36, 54]. For simplicity, we have assumed that hcp and fcc sites are equidistant and energetically equivalent. Furthermore, we consider the asymptotic case of infinite spring strengths, whose validity has been discussed in previous work [55]. In this case, the only boundary condition is that the first atom of the FK chain is fixed in a trough of the substrate potential (corresponding to the first atom which is not a surface atom as shown in the inset of figure 14). Since the fundamental FK parameter P_0 [36] which defines the misfit between the surface and the bulk atoms is not known for the Au(11, 9, 9) reconstruction, we assume that the atomic surface density should be similar to the Au(111) reconstructed surface and thus we take $P_0 = 22$. The graph of E_1, shown in figure 14, displays several minima which correspond to terrace widths locked by the reconstruction. For a vicinal surface, the surface energy per unit area also includes the step energy cost $E_2 = B/L$ and the repulsive elastic interaction energy between steps, $E_3 = C/L^3$. These contributions, where B and C have been deduced from the experimental data of Wang and Wynblatt [22], are also shown in figure 14. The curve of the total energy per unit area E clearly displays an additional minimum associated with unreconstructed terraces, 1.4 nm wide. Finally, the total energy curve is not convex and the tie bar construction applied to a Au(11, 9, 9) surface predicts that a phase separation will occur between one reconstructed phase composed of 6.5 nm wide terraces with a discommensuration line parallel to the steps and a non-reconstructed phase with terraces 1.4 nm wide. This is indeed in good agreement with our observations. The value of the reconstructed terraces could certainly be improved by taking into account the real shape of the potential and the non-asymptotic case. However, as P_0 is not perfectly known, we believe that this simple feature gives all the physical arguments for the understanding of faceting. In particular, it is in good agreement with the finding that the Au(322) is a stable non-reconstructed surface. Indeed, the value for the non-reconstructed terrace width is less sensitive than reconstructed terrace width to refinements in E_1.

The model predicts the instability of the Au(12, 11, 11) surface. The surface should separate into two reconstructed phases: (i) small terraces with one line of discommensuration,

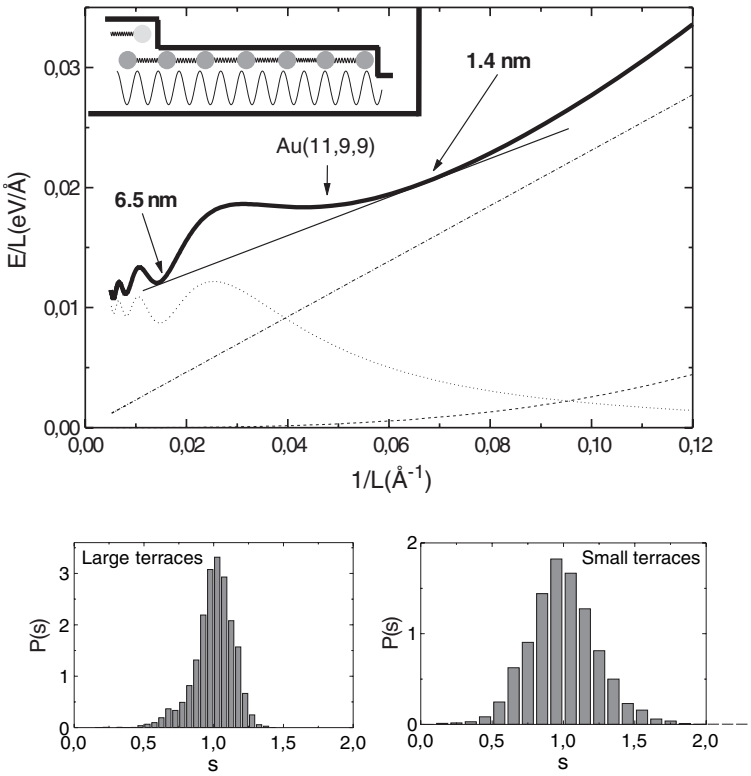

Figure 14. Upper part: calculated energy E per unit area of a Au(111) vicinal surface with {100} steps. We have also drawn the stressed terrace energy E_1, the step energy contribution E_2 and the the energy E_3 due to the elastic interaction between steps. E_1 is calculated using the FK model schematically represented in the inset. The tie construction which explains the vicinal surface faceting behaviour is also indicated. Lower part: experimental terrace width distribution measured for the large and small terraces found on Au(11, 9, 9).

and (ii) large terraces with two lines. The first phase is indeed observed (see figure 11(a)). The model therefore enables us to predict the stability of the (988) surface with one discommensuration line parallel to the steps on each terrace. However, the observed atomic structure of the large terraces on the faceted Au(12, 11, 11) is more complicated as seen in figures 11(b) and (c). We have explained it by a minimization of step energy which is not taken into account in our model. Furthermore, our model is purely one dimensional, whereas larger terraces display a 2D pattern for the reconstruction.

Finally, another remark concerns the prediction of the model compared to experimental measurements. We want to point out that the two local minima 6.5 and 1.4 nm associated with the tie bar construction discussed above do not have the same physical origin. One is clearly associated with a magic vicinal locking since it corresponds to a local minimum in the FK curve. On the other hand, the second minimum (at 1.4 nm) is just due to the competition between E_1 and E_2. Therefore, the convexity of these two minima is not the same. This effect can be seen experimentally studying the terrace width fluctuations [56]. One can observe that the smaller terraces have larger fluctuations than the larger terraces (see figure 14). This is in agreement with the fact that the second derivative of the total energy curve for the first minimum is smaller than for the second one.

As a conclusion, this simple model gives all the physical arguments for understanding the faceting phenomena and gives a reasonable quantitative agreement with the experiment. It definitively explains the value for the unreconstructed terrace width. The stability and the atomic structure of the (988) surface is also clearly understood within this model. More generally, it is the first time that a purely analytical model of FK type has given a good description for faceting phenomena. Furthermore, this approach explains the close relationship between the microscopic surface structure and the faceting process in order to understand how the reconstruction can lock some terrace widths.

5.2. Model of faceting for vicinals with {111} step edges

In the case of {111} step vicinal surfaces, reconstructed terraces consist in discommensuration lines crossing the step perpendicularly to the step edges. The step lattice breaks the symmetry of the three possible domains known for the $22 \times \sqrt{3}$ reconstruction and one only is stabilized. We have to note that the stress relief associated with the reconstruction occurs in the direction parallel to the steps and we do not expect any modulation of the reconstructed terrace energy as a function of its width. Therefore, instead of the previous FK model, we will rather consider the one initially proposed by Williams and Jeong [57, 14] in order to explain the faceting of Si (111) vicinal surfaces driven by the (7×7) reconstruction. This model is well suited when the reference plane exists in two different structural phases (here the $22 \times \sqrt{3}$ reconstruction and the (1×1) terraces, respectively for large and small terraces). Each phase can individually be described by a curve of the form of equation (1) without the quadratic term and with different values of the parameters. Thus, we write

$$\gamma_{\mathrm{R}}(\theta) = \gamma_{0,\mathrm{R}} + \frac{\beta_{\mathrm{R}}}{h}|\tan\theta| + g_{\mathrm{R}}|\tan\theta|^3 \tag{2}$$

and

$$\gamma_{\mathrm{NR}}(\theta) = \gamma_{0,\mathrm{NR}} + \frac{\beta_{\mathrm{NR}}}{h}|\tan\theta| + g_{\mathrm{NR}}|\tan\theta|^3 \tag{3}$$

where R and NR identify respectively the reconstructed and non-reconstructed phases. $\gamma_{0,\mathrm{R}} < \gamma_{0,\mathrm{NR}}$ since the reconstruction on the low index Au(111) surface lowers its free energy relative to that of an unreconstructed surface [40]. Reasonable assumptions are necessary, as already used in the case of Si(111) vicinal surfaces driven by the (7×7) reconstruction [57, 14]. We assume that $g_{\mathrm{R}} = g_{\mathrm{NR}}$. Then, if $\beta_{\mathrm{R}} > \beta_{\mathrm{NR}}$, the free energy curves intersect each other. This means that the existence of the reconstruction increases the step free energy. Since steps are crossed by the reconstruction, their atomic structure is disturbed and therefore it is reasonable to assume that their energy can only increase. Indeed, without the reconstruction, the steps have the lowest step energy due to their initial {111} microfaceted structure. More generally, since a step is a one-dimensional object, compared to a surface which is two dimensional, it can be assumed that the atomic rearrangement leading to a minimization of the free energy of the surface does not lower the step energy. As a result, the two curves intersect each other and the envelope of the two curves loses overall convexity. Thus phase separation will occur between two phases determined by the usual tie bar construction as illustrated in figure 15, where the parameter values have been calculated in order to describe both the stability of the Au(788) and the instability of the Au(455) surface.

Taking the value $g_{\mathrm{R}} = g_{\mathrm{NR}} = 68$ meV Å^{-2} fitted from the gold crystallite equilibrium shape [22], we deduce the value of $\Delta\gamma_0 = \gamma_{0,\mathrm{NR}} - \gamma_{0,\mathrm{R}}$ and $\Delta\beta = \beta_{\mathrm{R}} - \beta_{\mathrm{NR}}$ which allows us to describe a phase transition into a $\theta_{\mathrm{A}} = 4.0°$ vicinal phase and a $\theta_{\mathrm{B}} = 10.0°$ vicinal phase with

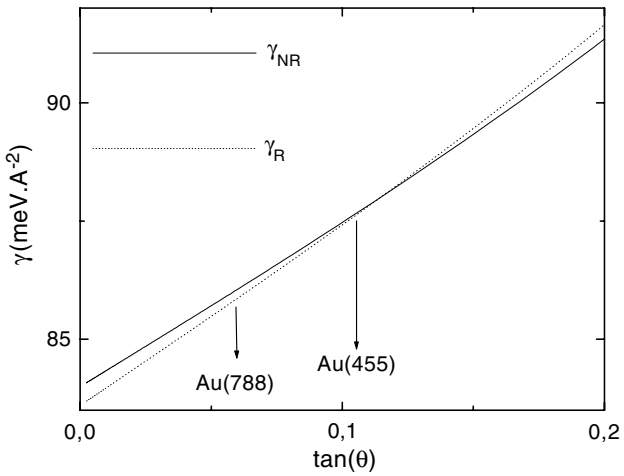

Figure 15. Surface energy as a function of the step density. The full line represents the energy of a non-reconstructed surface and the dotted line represents the energy of a reconstructed surface.

respect to the (111) orientation. Resolving the geometric equation for the tie bar condition, we find

$$\Delta\gamma_0 = 2g(\tan^3\theta_B - \tan^3\theta_A) \tag{4}$$

and

$$\Delta\beta = 3gh(\tan^2\theta_B - \tan^2\theta_A). \tag{5}$$

$h = 2.35$ Å is the monatomic step height on a Au(111) surface. $\Delta\gamma_0 = 0.7$ meV Å^{-2} and $\Delta\beta = 12.5$ meV Å^{-1} are found. These values depend on g, for which the value can be discussed. From the fit of the equilibrium shape of gold crystallites, $\gamma_0 = 84$ meV Å^{-2} and $\beta = 80$ meV Å^{-1}. The gain in surface energy due to the reconstruction is very small but consistent with previous investigations [58, 59]. It is worth noting that this experimental value does not take into account the further energy minimization due to the secondary herringbone reconstruction [39]. The variation in step energy is much higher and thus raises the question of why the discommensuration lines cross these step edges. We have already shown that in the case of {100} steps, modifying locally the reconstruction leads to a decrease of the step energy. In the case of {111} steps, in order to decrease the step energy, the lines have to avoid the step edge in the upper terrace together within the lower terrace (non-reconstructed {111} step). But this will cost surface free energy, and therefore a fine balance between the step energy and the surface energy will take place, which is not taken into account precisely in our model. Finally, the values found for $\Delta\gamma_0$ and $\Delta\beta$ sound reasonable and we believe that the mechanism explained above is responsible for the faceting of {111} step vicinal surfaces. Experimental determination or calculation for $\Delta\gamma_0$ and $\Delta\beta$ would validate or disprove this model.

6. Phase diagram and magic vicinals

Combining knowledge from experimental observations on Au(111) vicinal surfaces and models for the origin of faceting, we can summarize the stability of surfaces misoriented between 2° and 12° in two opposite azimuths. Of course, we are not considering a real phase diagram in the sense that we have not studied the morphology temperature dependence. Thus, what

we call stable is the morphology obtained after the *in situ* preparation described above. We believe this is representative of an equilibrium morphology obtained at 700 K.

When the surfaces are cut towards $[2\bar{1}\bar{1}]$, exhibiting {100} microfaceted steps, due to the FK model, only a few surfaces are stable between 1.7° and 11.4°: Au(755) and Au(322) are not reconstructed, whereas Au(988) and Au(17, 16, 16) are reconstructed. For Au(988), the reconstruction consists in one single line of discommensuration parallel to the steps located almost in the middle of each terrace.

This means that the majority of surfaces are unstable and will present a faceted morphology under the standard preparation in UHV. We expect that surfaces misoriented by a vicinal angle between 1.7° and 3.2° will separate into two reconstructed vicinal portions whose angles are 1.7° and 3.2°. Due to the possible number of atomic rows, this result concerns about 15 different vicinal surfaces. When the angle of misorientation lie between 3.2° and 9.4°, there is evidence that the surface will separate into area with terraces similar to the terraces of the (988) surface and a area with non-reconstructed terraces similar to the terraces of the (755) surface.

In the opposite azimuth, the model proposed for explaining the faceting phenomena is different. The instability diagram is restricted between 4.0° and 10.0°. We expect that all vicinals between 4.0° and 2.3° (Au(11, 12, 12)) are stable and reconstructed with discommensuration lines crossing the steps perpendicularly as observed for the (788) and (11, 12, 12) surfaces. This corresponds to about ten different vicinals. The 4.0° surface should be stable but as far as we know it has not yet been observed. This nominal (677) surface should display two atomic rows less than the (788). On the other hand, all vicinals steeper than the (233) surface should be stable and unreconstructed. Our model also predicts that surfaces below 2.3° are stable. However, for a low miscut angle, we expect to find the herringbone structure of the Au(111) reconstruction. The energy minimization associated with this structure may lead to some faceting phenomena which are not included in our model and, therefore, we cannot make any reliable predictions for miscut smaller than 2.3°.

Let us compare these results with what is known on the stability of Au(111) vicinals. If we compare with observations of equilibrium shape, we cannot explain the discontinuity angle at the sharp edges of the Au(111) facet. This angle has been found to be either 15° by Heyraud and Metois [60, 61], 19° by Wang and Wynblatt [22] or 21° more recently [23]. It is in any case much greater than the stable vicinal surfaces found here. This raises the question of the comparison between ECS and flat vicinal surfaces. Experiments performed on periodic annealed profiles have revealed the existence of stable facets whose angles are 3.7° and 11.7°. Although these angles are close to those of (322), (788) and (988) stable orientations, others are lacking for complete consistency. Maybe the resolution on such systems, both ECS and periodic profiles, is not sufficient to identify all orientations. Also, as far as we know such experiments have not reported any differences related to the azimuths. Other magic Au(111) vicinals have been predicted [62] or reported [25] but the azimuths were different.

7. Mesoscopic self-ordering on Au(111) vicinal surfaces

7.1. Introduction

Self-ordering on solid surfaces has been recognized as a promising alternative for growing uniform nanostructures with regular sizes and spacings [63, 64]. Despite the fact that a great variety of systems and geometries are concerned [65–67], long range elastic interaction is the common physical driving force of this phenomenon [68]. Spontaneous periodically faceted morphology has been reported for stepped surfaces at equilibrium [53, 1, 69, 57, 70, 29]. In this case, the elastic strain field results from a discontinuity of the intrinsic surface stress

tensor which appears on the facet frontier [68, 44]. A theoretical prediction is that, in such surfaces, the period results from a compromise between the energy gain induced by bulk elastic relaxation and the local energy cost of the facet edges [44]. However, although a lot of work has been concentrated on elastic relaxations, little is known about boundary energy terms. The self-ordering of Au(111) vicinal surfaces provides a unique opportunity to point out the crucial role of the boundary energy cost.

We have seen above that the mesoscopic order on these surfaces drastically varies with different vicinals [29], ranging from 10 to 500 nm. We compare pairs of surfaces which are misoriented by a similar angle with respect to (111) but in opposite azimuths. This is the case for Au(11, 9, 9) and Au(455), for which the vicinal angle is about 6°. The Au(11, 9, 9) surface is misoriented by a 5.57° angle towards the $[2\bar{1}\bar{1}]$ azimuth, and presents {100} steps. The Au(455) surface is misoriented by a similar angle, 5.76°, but towards the opposite azimuth, thus it presents {111} steps. The faceting of these surfaces displays periodically faceted morphology with different periods: a 180 nm period is observed on Au(455) whereas a shorter 7 nm period is obtained on Au(11, 9, 9). There is a factor of 25 between both periods of faceting. In the following we examine how the atomic structure interplays with the mesoscopic order using the elastic continuum model proposed by Marchenko [44].

When a phase separation occurs on a vicinal surface, the discontinuities of the surface stress tensor at the edges between two facets generate lines of local forces which lead to long range bulk elastic relaxations (see figure 16). Marchenko demonstrated that, in order to minimize the elastic energy, the surface morphology evolves towards the lowest possible period. However, there is a competition between this elastic energy gain and the local edge energy cost, C_1. The order of magnitude of the period is given by $\kappa = 2\pi a \exp(1 + C_1/C_2)$, where a is an atomic cut-off distance, and C_2 evaluates the bulk elastic relaxations [44].

7.2. Elastic energy gain

The first step is to evaluate the elastic energy gain C_2. $C_2 = ((1 - \nu^2)F^2)/(\pi Y)$ where ν is the Poisson ratio and Y is the Young modulus. The force F per unit length exerted on the edge between two adjacent facets with different stresses $\sigma_{\mathbf{A}}$ and $\sigma_{\mathbf{B}}$ is $\mathbf{F} = \sigma_{\mathbf{A}} + \sigma_{\mathbf{B}}$ (see figure 16). The elastic energy gain is therefore related to the surface stress tensor of each facet forming the hill-and-valley structure. Molecular dynamics calculations have been performed in order to evaluate the surface stress of vicinal surfaces versus the step density for both azimuths studied here. Results are shown in figure 17. This simulation does not take into account surface reconstructions which are able to lower the surface stress. On Au(111), it has been found that the surface stress is 20% smaller on the reconstructed surface than on the unreconstructed surface [40]. Using the curves of figure 17, we can evaluate the forces located at the edges of facets on the Au(111) vicinals studied here. We take the Au(111) surface stress value $\sigma_0 = 173$ meV Å^{-2} [71] as reference, which has been calculated for a non-reconstructed surface. In the case where the terraces are reconstructed (i.e. Au(11, 9, 9) and Au(12, 11, 11)), we will take the value of the surface stress to be 20% lower. Knowing the crystallographic orientation of each facet, we can evaluate the elastic energy gain C_2. Values are reported in table 3 (A denotes the less misoriented facet whereas B is the more misoriented one).

7.3. Role of the edge energy in the mesoscopic order

The elastic energy gain being evaluated, it is now necessary to estimate the local edge energy cost C_1. We will first calculate C_1 for Au(455) and Au(11, 9, 9) which are the model surfaces detailed here. The precise knowledge of the surface atomic structure allows us to estimate the local energy cost C_1 to insert one phase into the other. This insertion is schematically shown

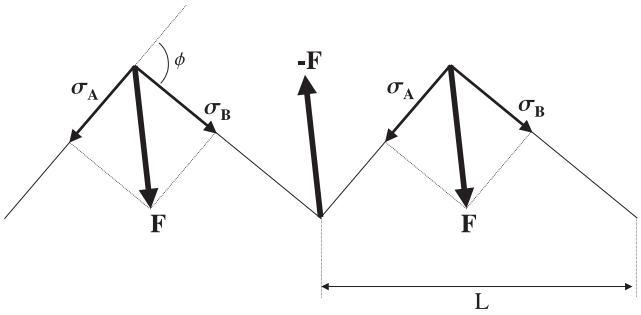

Figure 16. Scheme for a faceted periodic morphology, showing the surface stresses of facets (from [29]).

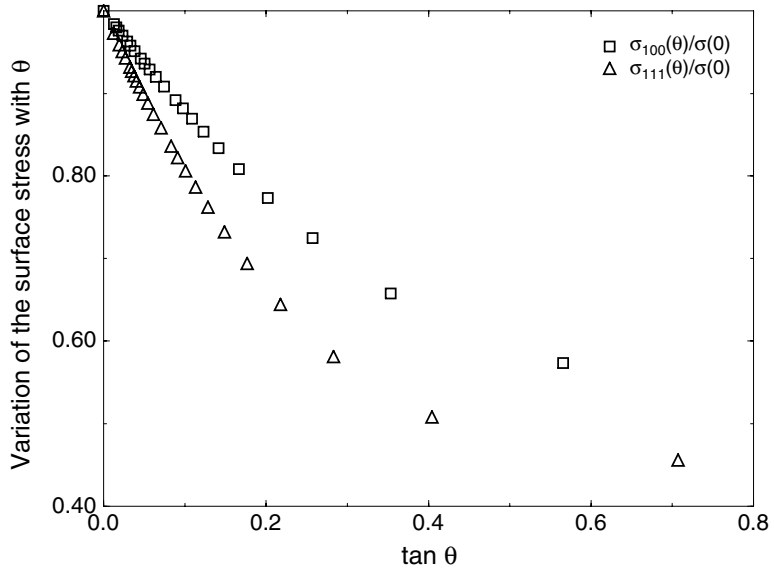

Figure 17. Atomistic calculations for the variation of the surface stress σ on vicinals of Au(111) with miscut around the $[1\bar{1}0]$ direction. (△) vicinals with {111} steps, (□) vicinals with {100} steps (from [29]).

Table 3. Calculated surface stresses σ_A and σ_B for each faceted surfaces. From these values we deduce F, which is the force per unit length exerted on the facet edge and C_{elas} which is the energetic character called C_2 in the text.

	σ_A (meV Å^{-2})	σ_B (meV Å^{-2})	F (pN at.$^{-1}$)	C_{elas} (meV Å^{-1})
Au(455)	149	126	115	0.3
Au(11, 9, 9)	165	142	130	0.4
Au(12, 11, 11)	170	165	29	0.02

in figure 18 where step configurations are drawn before (upper part) and after (lower part) one phase has been inserted into the other. By definition, C_1 is the difference between the surface energies of the two configurations ignoring the elastic contribution, which is already taken into account via the C_2 parameter. The term of first order is the difference in step energies.

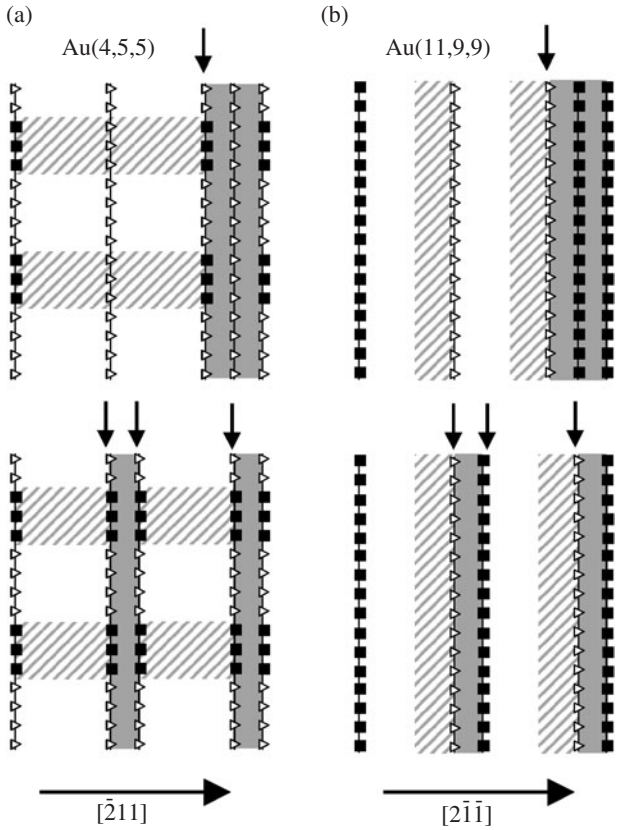

Figure 18. Spontaneous periodic faceting of vicinals with {111} steps (a) and vicinals with {100} steps (b). In each case a schematic step arrangement configuration before (upper part) and after (lower part) one phase has been inserted into the other is drawn. The two terraces of the unreconstructed phase are in grey (i.e. they have an fcc stacking). The hcp atomic stacking fault on the two terraces of the reconstructed phase is represented by a hatched area. Arrows indicate edges between vicinal phases. Step structures are indicated by triangles for {111} steps and full black squares for {100} steps (from [2]).

It can be seen in figure 18(a) that inserting one phase into the other for Au(455) transforms two {111} steps into a periodic succession of {111} and {100} step portions. Due to the higher step energy for the {100} steps, this result in a local energy cost C_1. An estimation of this term using the {111} and {100} step energies [22, 47] as well as the proportion of hcp stacking along the step gives a few meV Å^{-1}. Following Marchenko's model, it leads to a micronic period for vicinal surfaces with {111} steps, not far from our observations of about 200 nm. However, it is not expected to obtain a quantitative agreement, taking into account the roughness of our estimation together with the very high sensitivity of the exponential function. More interesting is the comparison with the Au(11, 9, 9) surface. Indeed, comparing steps in the upper and lower parts of figure 18(b) shows that no difference in step energies appears when one phase is inserted into the other. In this case, additional effects must be invoked to evaluate C_1. It has been recently proposed that C_1 could result from the modification of the terrace widths in the vicinity of the frontier due to its asymmetric environment [66]. Following this work, we assumed a few per cent variation of the edge terraces so that the edge energy cost

can be evaluated from our FK model. It is found to be a few tenths of meV $Å^{-1}$. This value is probably overestimated since the calculations of Liu *et al* concern a much more asymmetric case than ours. However, this gives an upper limit for C_1 which is at the most equal to C_2. Thus, Marchenko's model predicts the smallest possible period that can be realized with the two favoured terrace widths. This is indeed what we observe on the Au(11, 9, 9) surface. Of course, the validity of the Marchenko model has to be discussed in the case of such a small phase extent but it is known that the elastic theory provides correct results until a few atomic distances. Therefore, our results strongly suggest that the difference in C_1 between both types of vicinal Au(11, 9, 9) and Au(455) is responsible for their drastically different mesoscopic faceted morphologies. Thus, Au(111) vicinal surfaces provide a unique opportunity to point out the crucial role played by the boundary energy cost in the self-ordering phenomena [2]. Surprisingly, although the edge energy cost is not the driving force for the periodic faceting, it is able to monitor the value of the period. This is indeed of primordial interest for numerous applications of self-ordered systems.

Now, let us examine the more complex case of Au(12, 11, 11). Difficulty arises due to the fact that the atomic structure of the largest terraces found on the faceted morphology changes depending on whether it is close to the facet edge or not. The large terraces display more frequently the complex structure shown in figure 11(c) and called 'structure c' below. However, the so-called 'viaduct' or 'b' structure (see figure 11(b)) is always found in the vicinity of the smallest terrace phase. Understanding the periodicity in this case is much complicated since now the surface free energy is changing with the hill-and-valley periodicity, which has not been taken into account previously. Two possibilities can apply. When both structures have almost the same energy, the surface will seek the smallest period possible. Indeed, the edge energy cost between the 'viaduct' structure and the small reconstructed terrace is of the same order of magnitude as in the case of Au(11, 9, 9) for the same structural reasons. When there is an energetic difference between both structures, the largest terrace phase will display only the complex structure c (except very close to the small terrace in order not to perturb such a small terrace phase). In this case, the period will be great, since having the smallest period will have a cost in energy due to the creation of more b structure. Unfortunately, we do not know the difference in energy between structures b and c. However, it is worth noting that the very small value of C_2 for this particular surface justifies the large periodicity indeed observed.

8. Application for self-assembled growth of nanostructures

Achieving a high degree of order in periodic arrays of uniform nanometre size clusters has become one of the greatest solid state physics challenges in the last few years. Methods for assembling arbitrary atomic scale structures have been proposed involving scanning probe assisted lithography [72]. Another promising way is to use self-organization phenomena [68, 73]. The advantage of this parallel processing technique is to organize regular nanostructures over macroscopic areas with a high spatial density. It has been demonstrated that strained-relief patterned substrates such as dislocation networks can serve as templates for growing uniform regularly spaced nanostructures [64, 74, 75, 63, 76, 77]. However, intrinsic defects such as step edges hamper the achievement of long range ordered arrays of nanostructures since steps are often the main defect killing the surface dislocation network's coherence. Steps can also favour large cluster growth which hinders the uniformity of nanostructure sizes. Since macroscopic averaging methods are still commonly used for measuring physical properties of the nanostructures, these defects represent major drawbacks. In order to overcome these difficulties, we proposed recently a novel approach based on strain relief *vicinal* patterned substrates for two-dimensional (2D) self-ordered growth.

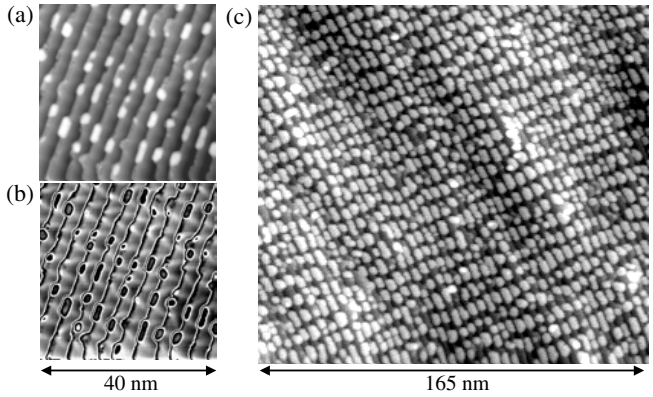

Figure 19. STM images of Co on Au(788) at room temperature. (a) Raw image of 0.15 ML coverage of Co on Au(788). (b) The corrugation due to terrace levels has been subtracted in order to observe the island positions compared to the discommensuration lines. (c) 0.4 ML of Co on Au(788).

The basic idea is taking advantage of different morphology found on Au(111) vicinal surfaces in order to use these surfaces as templates for the growth of organized nanostructures. Using vicinal surfaces as templates was originally proposed for achieving the growth of nanowires, and therefore entering the world of one-dimensional nanostructures [78]. Magnetic Fe nanowires have be grown on stepped W(110) [79] and have been investigated by spin-polarized STM [80]. Recently, Co atomic chains have been achieved by decoration of a vicinal Pt surface [81] and ferromagnetism has been measured in such chains [82]. The main characteristic of vicinal surfaces is that the step array keeps its coherence over the whole sample which is of macroscopic size. Here we want to combine the vicinal step array with a strain relief pattern which will result in a 2D self-ordered growth with long range order. Best candidates for such 2D growth have been found to be the Au(111) vicinal surfaces cut in the $[\bar{2}11]$ azimuth, whose steps exhibit $\{111\}$ microfacets, and with misorientation angle lying between 2° and 4°. Prototypes are Au(11, 12, 12) and Au(788) orientations described in section 4.

We recall that the Au(788) surface is patterned in two dimensions:

(i) along the $[\bar{2}11]$ direction, the periodicity is the terrace width 3.9 nm and can be changed with a different miscut angle [50];
(ii) along the $[01\bar{1}]$ direction, the periodicity is 7.2 nm, fixed by the reconstruction, and does not vary significantly with the miscut angle.

The LEED pattern indicates the good long range order (on a macroscopic scale) of both the stepped surface and the reconstruction since we can see up to the third diffraction peak order in both directions. This is a major difference from the earlier works on self-organized growth obtained using dislocation networks on close-packed surfaces as templates [64, 75, 63, 76, 77, 74].

Due to a place exchange mechanism at the crossing of the reconstruction lines and the step edges a 2D superlattice of two monolayer (ML) high cobalt nanodots is grown on the Au(788) surface at room temperature (see figure 19(b)). Although the advantage of using such a substrate is to improve the long range order of the organized growth, there are a lot of local defects in the organized structure and the island size distribution achieved at room temperature is not very sharp [51].

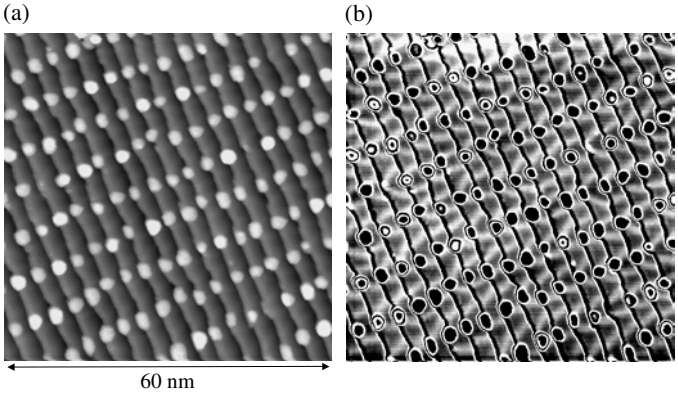

Figure 20. Details of the 0.2 ML deposition of Co on Au(788) at 130 K. (a) Raw STM image. (b) The corrugation due to terrace levels has been subtracted in order to observe the island positions compared to the discommensuration lines (from [90]).

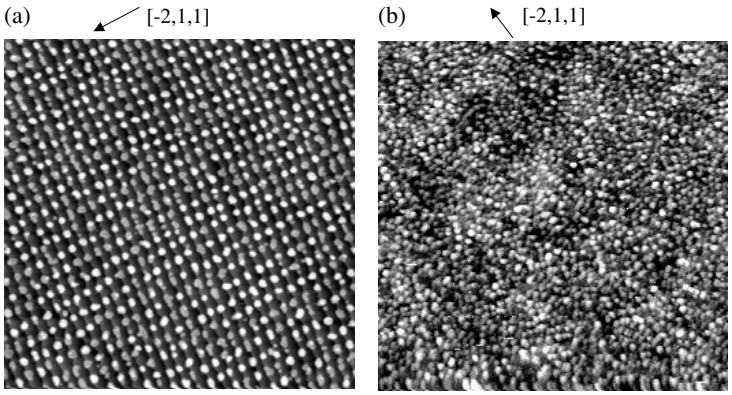

Figure 21. (a) STM image (175×175 nm^2) of 0.4 ML deposition of cobalt at room temperature on Au(11, 12, 12). (b) STM image (150×150 nm^2) of 0.4 ML deposition of cobalt at room temperature on Au(233) (from [91]).

In order to improve the local order of this dot array we have performed experiments with different substrate temperatures. It has been shown in the Ag/Ag(2 ML)/Pt(111) system that lowering the deposition substrate temperature can inhibit some diffusion processes across discommensuration lines and so leads to an organized growth [64]. In this case, Brune *et al* [64] found that $T \simeq 110$ K is the best temperature to get a well ordered array. Following this idea, we have deposited a sub-monolayer coverage of Co on Au(788) cooled down to 130 K. Since we have taken the subsequent STM images at room temperature, we could expect a different arrangement compared to the non-annealed case. Figure 20 shows an STM image of the cobalt growth. At a first glance, it looks like a perfect rectangular array of nanodots. We can estimate over many images that the proportion of defects in this array is about 1%. Few micron areas show the same perfection of island organization [51]. The island size distribution is narrower than that measured for the room temperature deposition on Au(788) and even on Au(111).

It is interesting to remark that the terrace width value can be monitored very easily by changing the surface misorientation angle. This degree of freedom allows us to tune one of

the periodicities of the cobalt dot array. This is illustrated by the case of the Au(11, 12, 12) substrate where we obtain an almost square cell for the dot array as shown in figure 21(a). In this case the terrace width is 5.6 nm which is close to the reconstruction period. For interacting nanostructures (magnetic dipolar interactions, elastic interactions via the substrate, . . .) the isotropy of the superlattice is an important parameter. Although this is of great interest to vary the symmetry of the lattice cell one has to be careful that changing the terrace width can be destructive for the strain relief pattern. In figure 21(b) we show the example of cobalt deposition on the Au(233) surface. In this case the terrace width is 1.4 nm, a value that does not lead to a reconstruction within the terraces. As a consequence, we observe no organization when the cobalt deposition is performed on this substrate (see figure 21(b)).

9. Conclusions

In this paper, we have given a complete overview of our recent work on Au(111) *vicinal* surfaces. Special emphasis has been placed on the self-ordering properties. Since gold surfaces are commonly used as substrates in a wide variety of fields, such as organic molecules [83], magnetism [84] or heterogeneous catalysis [77], vicinal surfaces are ideal templates for nanostructuring applications, since they provide periods between 1 and 100 nm, with a coherence over the whole macroscopic samples. We have shown in detail what morphologies can be expected by using gold vicinal surfaces.

(i) Regular vicinals with step periodicity between 1 and 4 nm. Terraces are reconstructed or not.
(ii) Faceted morphologies allow us to vary the long range order periodicity between 5 and 500 nm.

The key point in understanding these morphologies comes from the interaction between reconstruction and step edges. Elucidating this interaction leads to two fundamental consequences:

(i) two different models have proposed for understanding the faceting properties and
(ii) the mesoscopic faceting periodicity has been linked to the local atomic order of the facet edge.

Open questions on Au(111) vicinal surfaces are still

(i) the comparison with the gold crystallite equilibrium shape which displays large angles of discontinuity at the Au(111) facet sharp edges [20–23],
(ii) the comparison with the magic vicinal obtained from annealed periodic profiles [24] and
(iii) the temperature behaviour and the role of the phase transition towards the fluid phase [41, 42].

However, we have shown that reconstructed vicinal surfaces are well suited for 2D growth of nanostructures. Gold vicinal surfaces spontaneously exhibit such a pattern but it is likely that every well known epitaxial dislocation network (metal systems [85–87, 64], and also semiconductors [88, 89]) will display similar patterns on vicinal surfaces.

Acknowledgments

This work has been supported by the Conseil Régional d'Ile de France (CRIF) and the Université Paris 7. Co-workers J M Berroir, B Croset, H Ellmer, V Etgens, P Hecquet, J Klein, S Gauthier, F Pourmir and B Salanon who have contributed to the work presented here are acknowledged. Discussions with P Zeppenfeld, C Cohen and L Barbier were very helpful.

References

[1] Song S, Yoon M, Mochrie S, Stephenson G and Milner S 1997 *Surf. Sci.* **372** 37
[2] Repain V, Berroir J, Croset B, Rousset S, Garreau Y, Etgens V and Lecoeur J 2000 *Phys. Rev. Lett.* **84** 5367
[3] Rosenhain W 1902 *Proc. R. Soc.* A **70** 252
[4] Rosenhain W and Ewen D 1912 *J. Inst. Met.* **8** 149
[5] Fonda G 1923 *Phys. Rev.* **21** 343
[6] Stephanopoulos M F and Schmidt L 1979 *Prog. Surf. Sci.* **9** 83
[7] Moore A 1963 *Metal Surfaces* vol 256, ed W D Robertson and N A Gjostein (Metals Park, OH: American Society for Metals) p 155
[8] Wulff G 1901 *Z. Kristallogr.* **34** 449
[9] Herring C 1951 *Phys. Rev.* **82** 87
[10] Watson G, Gibbs D, Zehner D, Yoon M and Mochrie S 1998 *Surf. Sci.* **407** 59
[11] Yoon M, Mochrie S, Zehner D, Watson G and Gibbs D 1994 *Phys. Rev.* B **49** 16702
[12] Song S and Mochrie S 1994 *Phys. Rev. Lett.* **73** 995
[13] Song S, Mochrie S and Stephenson G 1995 *Phys. Rev. Lett.* **74** 5240
[14] Jeong H and Williams E 1999 *Surf. Sci. Rep.* **34** 171
[15] Phaneuf R, Williams E and Bartelt N 1988 *Phys. Rev.* B **38** 1984
[16] Phaneuf R, Williams E and Bartelt N 1987 *Phys. Rev. Lett.* **58** 2563
[17] Samson Y, Rousset S, Gauthier S and Klein J 1994 *Surf. Sci.* **315** L969
[18] Sotto M and Boulliard J 1989 *Surf. Sci.* **214** 97
[19] Bartolini A, Ercolessi F and Tossati E 1989 *Phys. Rev. Lett.* **63** 872
[20] Heyraud J and Metois J 1980 *J. Cryst. Growth* **50** 571
[21] Heyraud J and Metois J 1980 *Acta Metall.* **28** 1789
[22] Wang Z and Wynblatt P 1998 *Surf. Sci.* **398** 259
[23] Emundts A, Bonzel H, Wynblatt P, Thürmer K, Reutt-Robey J and Williams E 2001 *Surf. Sci.* **481** 13
[24] Bonzel H, Breuer U, Voigtländer B and Zeldov E 1992 *Surf. Sci.* **272** 10
[25] Watson G M, Gibbs D, Song S, Sandy A, Mochrie S and Zehner D M 1995 *Phys. Rev.* B **52** 12329
[26] Rousset S, Berroir J, Repain V, Garreau Y, Etgens V, Lecoeur J and Pinchaux R 1999 *Surf. Sci.* **443** 265
[27] Garreau Y, Repain V, Berroir J, Rousset S, Etgens V and Lecoeur J 2000 *Physica* B **283** 223
[28] Pourmir F, Rousset S, Gauthier S, Sotto M, Klein J, Lecoeur J and Bellier J 1995 *Surf. Sci.* **324** L337
[29] Rousset S, Pourmir F, Berroir J, Klein J, Lecoeur J, Hecquet P and Salanon B 1999 *Surf. Sci.* **422** 33
[30] Lecoeur J and Bellier J 1992 *J. Electroanal. Chem.* **337** 197
[31] Lecoeur J and Rousset S 2002 *J. Electroanal. Chem.* **519** 18
[32] Harten U, Lahee A, Toennis J and Wöll C 1985 *Phys. Rev. Lett.* **54** 2619
[33] Wöll C, Chiang S, Wilson R and Lippel P 1989 *Phys. Rev.* B **39** 7988
[34] Barth J, Brune H, Ertl G and Behm R 1990 *Phys. Rev.* B **42** 9307
[35] Frenkel Y and Kontorova T 1938 *Zh. Eksp. Teor. Fiz.* **8** 1340
[36] Frank F and der Merwe J V 1948 *Proc. R. Soc.* A **198** 205
[37] El-Batanouny M, Burdick S, Martini K and Stancioff P 1987 *Phys. Rev. Lett.* **58** 2762
[38] Ravelo R and El-Batanouny M 1989 *Phys. Rev.* B **40** 9574
[39] Narasimhan S and Vanderbilt D 1992 *Phys. Rev. Lett.* **69** 1564
[40] Bach C, Giesen M, Ibach H and Einstein T 1997 *Phys. Rev. Lett.* **78** 4225
[41] Huang K, Gibbs D, Zehner D, Sandy A and Mochrie S 1990 *Phys. Rev. Lett.* **65** 3313
[42] Sandy A, Mochrie S, Zehner D, Huang K and Gibbs D 1991 *Phys. Rev.* B **43** 4667
[43] Abernathy D, Gibbs D, Grübel G, Huang K, Mochrie S, Sandy A and Zehner D 1993 *Surf. Sci.* **283** 260
[44] Marchenko V 1981 *Sov. Phys.—JETP* **54** 605
[45] Repain V, Berroir J, Rousset S and Lecoeur J 1999 *Europhys. Lett.* **47** 435
[46] Repain V, Berroir J, Rousset S and Lecoeur J 2000 *Appl. Surf. Sci.* **162/163** 30
[47] Michely T and Comsa G 1991 *Surf. Sci.* **256** 217
[48] Michely T, Besocke K and Comsa G 1990 *Surf. Sci.* **230** L135
[49] Mugarza A, Mascaraque A, Repain V, Rousset S, Altmann K, Himpsel F, Koroteev Y, Chulkov E, de Abajo F G and Ortega J E 2002 *Phys. Rev.* B **66** 245419
[50] Repain V, Berroir J, Rousset S and Lecoeur J 2000 *Surf. Sci.* **447** L152
[51] Repain V, Baudot G, Ellmer H and Rousset S 2002 *Europhys. Lett.* **58** 730
[52] Rousset S, Pourmir F, Gauthier S, Lacaze E, Sotto M, Klein J and Lecoeur J 1996 *J. Vac. Sci. Technol.* B **14** 1131
[53] Yoon M, Mochrie S, Zehner D, Watson G and Gibbs D 1995 *Surf. Sci.* **338** 225
[54] Mansfield M and Needs R 1990 *J. Phys.: Condens. Matter* **2** 2361

[55] Croset B and de Beauvais C 2000 *Phys. Rev.* B **61** 3039
[56] Einstein T and Pierre-Louis O 1999 *Surf. Sci.* **424** L299
[57] Williams E 1994 *Surf. Sci.* **299/300** 502
[58] Ibach H 1997 *Surf. Sci. Rep.* **29** 193
[59] Goyhenex C and Bulou H 2001 *Phys. Rev.* B **63** 235404
[60] Heyraud J and Metois J 1983 *Surf. Sci.* **128** 334
[61] Heyraud J and Metois J 1986 *Surf. Sci.* **177** 213
[62] Bilalbegovic G, Ercolessi F and Tossati E 1992 *Europhys. Lett.* **18** 163
[63] Chambliss D, Wilson R and Chiang S 1991 *Phys. Rev. Lett.* **66** 1721
[64] Brune H, Giovannini M, Bromann K and Kern K 1998 *Nature* **394** 451
[65] Fruchart O, Klaua M, Barthel J and Kirschner J 1999 *Phys. Rev. Lett.* **83** 2769
[66] Liu F, Tersoff J and Lagally M 1998 *Phys. Rev. Lett.* **80** 1268
[67] Teichert C 2002 *Phys. Rep.* **365** 335
[68] Shchukin V and Bimberg D 1999 *Rev. Mod. Phys.* **71** 1125
[69] Zuo J, Zehner D, Wendelken J, Warmack R and Yang H 1994 *Surf. Sci.* **301** 223
[70] Ozcomert J, Pai W, Bartelt N and Reutt-Robey J 1994 *Phys. Rev. Lett.* **72** 258
[71] Needs R and Mansfield M 1989 *J. Phys.: Condens. Matter* **1** 7555
[72] Eigler D and Schweizer E 1990 *Nature* **344** 524
[73] Sun S, Murray C, Weller D, Folks L and Moser A 2000 *Science* **287** 1989
[74] Voigtländer B, Meyer G and Amer N 1991 *Phys. Rev.* B **44** 10354
[75] Voigtländer B, Meyer G and Amer N 1991 *Surf. Sci.* **225** L529
[76] Altman E and Colton R 1994 *Surf. Sci.* **304** L400
[77] Stephenson A, Baddeley C, Tikhov M and Lambert R 1998 *Surf. Sci.* **398** 172
[78] Himpsel F, Ortega J, Mankey G and Willis R 1998 *Adv. Phys.* **47** 511
[79] Hauschild J, Elmers H and Gradmann U 1998 *Phys. Rev.* B **57** R677
[80] Pietzsch O, Kubetzka A, Bode M and Wiesendanger R 2000 *Phys. Rev. Lett.* **84** 5212
[81] Gambardella P, Blanc M, Bürgi L, Kuhnke K and Kern K 2000 *Surf. Sci.* **449** 93
[82] Gambardella P, Dallmeyer A, Maiti K, Malagoli M, Eberhardt W, Kern K and Carbone C 2002 *Nature* **416** 301
[83] Marchenko O and Cousty J 2000 *Phys. Rev. Lett.* **84** 5363
[84] Chappert C and Bruno P 1988 *J. Appl. Phys.* **64** 5736
[85] Barth J, Behm R and Ertl G 1995 *Surf. Sci.* **341** 62
[86] Meyer J, Schmid P and Behm R 1995 *Phys. Rev. Lett.* **74** 3864
[87] Günther C, Vrijmoeth J, Hwang R and Behm R 1995 *Phys. Rev. Lett.* **74** 754
[88] Horn-Von-Hoegen M, Falou A, Pietsch H, Müller B and Henzler M 1993 *Surf. Sci.* **298** 29
[89] Böhringer M, Molinas-Mata P, Artacho E and Zegenhagen J 1995 *Phys. Rev.* B **51** 9965
[90] Repain V, Baudot G, Ellmer H and Rousset S 2002 *Mater. Sci. Eng.* B **96** 178
[91] Baudot G, Rohart S, Repain V, Ellmer H, Girard Y and Rousset S 2003 *Appl. Surf. Sci.* **212/213** 360